Water Resources Research

RESEARCH ARTICLE
10.1029/2021WR030239

Systematic Evaluation of Geometry-Driven Lateral River-Groundwater Exchange in Floodplains

Jonas Allgeier[1], Simon Martin[1], and Olaf A. Cirpka[1]

[1]Center for Applied Geoscience, University of Tübingen, Tübingen, Germany

Key Points:

- We develop a semi-analytical solution describing lateral exchange between rivers and floodplain aquifers driven by the valley geometry
- We investigate how the exchange flux, the area of the hyporheic zone, and travel times depend on geometric and hydraulic properties
- We derive simplified expressions allowing estimating these quantities as a preliminary step prior to detailed site investigations

Supporting Information:

Supporting Information may be found in the online version of this article.

Correspondence to:

O. A. Cirpka,
olaf.cirpka@uni-tuebingen.de

Citation:

Allgeier, J., Martin, S., & Cirpka, O. A. (2021). Systematic evaluation of geometry-driven lateral river-groundwater exchange in floodplains. *Water Resources Research*, *57*, e2021WR030239. https://doi.org/10.1029/2021WR030239

Received 19 APR 2021
Accepted 21 JUL 2021

Abstract The widening and narrowing of river-valley aquifers can cause valley-scale lateral hyporheic exchange even if the river is straight and its slope is uniform. For the aforementioned system, we derive a semi-analytical solution describing steady-state groundwater flow for a simplified two-dimensional geometry of the aquifer and uniform lateral influx from hillslopes. We use this solution to evaluate the geometry-driven lateral hyporheic exchange flux between the aquifer and the river. By systematically varying the model parameters, we decipher how this flux and the area of the exchange zone depend on geometric (e.g., minimum and maximum domain width) and hydrogeological parameters (e.g., hydraulic conductivity, ambient hydraulic gradient and lateral influxes). The results suggest pronounced hyporheic flow for cases with distinct widening behavior and small cross-sectional widths at the floodplain inlet and outlet. Furthermore, we analyze the travel-time distribution of water flowing through the exchange zone, which approximately follows a beta distribution. We express our findings in terms of simple proxy-equations that can be used to easily estimate the exchange flux, the area of the exchange zone, and the associated travel-time distribution for a given geographic/landscape setting.

1. Introduction

Floodplains are landscape elements that connect hillslopes, aquifers, and surface waters. Often their hydraulic and biogeochemical properties are of high importance for transport and transformation of solutes, because the elevated contents of organic carbon in floodplain sediments cause steep redox gradients when oxic water enters these zones (e.g., Bates et al., 2000; Clilverd et al., 2013; Cloke et al., 2003; Hill, 1990, 2019; Vidon et al., 2019; Woessner, 2000). Over the past decades, hydrogeological research has become aware of the necessity of jointly investigating surface and subsurface processes rather than treating them as separate domains (e.g., Winter et al., 1998). As a consequence, a key role in floodplain hydrogeology has been attributed to the interactions between aquifers and the connected rivers (e.g., Fritz et al., 2018; Ward et al., 2016; Ward & Packman, 2019). As summarized by Cook (2015), there are different types of such surface-water/groundwater interactions, comprising *river gain*: exfiltration/discharge of groundwater into the river, *river loss*: infiltration/recharge of river water into groundwater, *bank storage*: bidirectional exchange between river and groundwater due to dynamic changes in river-water stage, and *hyporheic exchange*: water originating from rivers, taking a detour through groundwater and coming back to the river without a net impact on the water balance of either the aquifer or the river. In recent studies specifically related to floodplain hydrology, hyporheic exchange has received significant attention, as it is important for various aspects of water quality and ecology, including microbial activity, solute turnover, nutrient fate, and redox conditions (Boano et al., 2009; Fabian et al., 2011; Hayashi & Rosenberry, 2002; Lewandowski et al., 2019; Triska et al., 1993; Ward, 2016).

1.1. Lateral Hyporheic Exchange

Hyporheic exchange occurs on different spatial and temporal scales (Barthel & Banzhaf, 2016; Boano et al., 2014; Magliozzi et al., 2017, 2018; Ward & Packman, 2019; Zachara et al., 2020), ranging from centimeter-scale exchange induced by bedforms, over meter-scale exchange between step-pool sequences, to kilometer-scale hyporheic exchange, which is sometimes referred to as parafluvial flow (Cook, 2015; Mallard et al., 2014). While small-scale exchange typically takes place in the vertical direction, larger-scale hyporheic exchange can also occur laterally (Fabian et al., 2011; Gooseff et al., 2003; Hayashi & Rosenberry, 2002; Wagner & Bretschko, 2003), for example, between river meanders (Boano et al., 2009; Gomez et al., 2012).

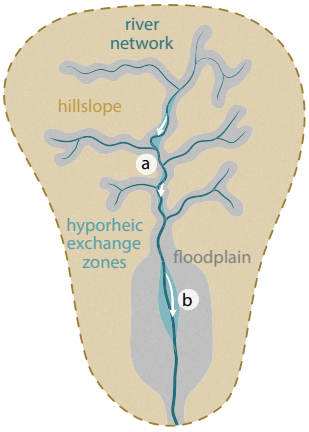

Figure 1. Conceptual drawing of large-scale, lateral, geometry-driven hyporheic exchange zones in a river catchment. (a) hyporheic exchange between river meanders (not part of this study), (b) hyporheic exchange in widening floodplains with straight (channelized) river section (focus of this study).

As shown by Tonina and Buffington (2009), changes in cross-sectional area of floodplain aquifers are one of three drivers for hyporheic exchange besides non-uniform hydraulic conductivity and changes in energy head gradients. It is quite typical for floodplain aquifers, to have a varying cross-sectional area in settings of alternating degrees of valley confinements. In geomorphology, the term "confined" typically is used to describe valleys with a narrow floodplain that are laterally bounded by steep flanks forming a typical V-shape (Baxter et al., 1999; Fotherby, 2009; Nagel et al., 2014). In contrast to that, unconfined valleys exhibit extensive floodplains and flat surface topography (Nagel et al., 2014). Hence, a sequence of confined and unconfined valleys along a stream, as described by Baxter et al. (1999) and Nagel et al. (2014), among others, results in lateral widening and narrowing of floodplain aquifers. Such sequences can form when alternating softer and harder rock layers of a stratigraphic sequence dip into the direction of flow so that the river alternatingly cuts through these softer and harder rocks. At the up- and downstream ends of an unconfined basin, the river is hindered to erode the harder bedrock, whereas the soft bedrock in between can be carved out by the river. The widened valley is then filled with fluvial sediments and hillslope material forming the floodplain aquifer. In fact, floodplain aquifers with narrow inlet and outlet cross-sections and a basin-shaped central section occur frequently (e.g., Castro & Hornberger, 1991; Clément et al., 2003; Helton et al., 2012; Martin et al., 2020; Ó Dochartaigh et al., 2019). As example, Ohara et al. (2018) developed a simplified procedure to approximate the boundary of floodplain aquifers solely from digital elevation models. They made use of the fact that the top surfaces of floodplains exhibit small slopes, and that floodplain boundaries are characterized by inflection points of surface elevation (i.e., where the curvature is zero). The mappings of Ohara et al. (2018) show a number of floodplain aquifers along the investigated stream network following the typical widening shape between connection points of small width.

As mentioned above, the widening geometry of an unconfined valley in the middle of two confined ones can sustain lateral hyporheic exchange on the valley-scale (Buffington & Tonina, 2009; Nagel et al., 2014; Tonina & Buffington, 2009). Where the valley widens, river water infiltrates into the aquifer, then flows predominantly downvalley, and is pushed back into the river where the valley narrows again (similar effects on vertical non-uniform cross-sections were already described by Vaux, 1968). This large-scale excursion of river water into the adjacent aquifer defines the riparian hyporheic-exchange zone from a hydrogeological perspective and is the main point of interest of the present study. Figure 1 schematically shows that alternating transitions from (partially) confined to unconfined valleys (and vice versa) can be a cause of lateral geometry-driven hyporheic exchange even in straight river reaches, which can often be found in anthropogenically modified, channelized floodplain systems (e.g., Brookes, 1987).

The actual quantitative measurement of hyporheic exchange in field studies (in terms of flux, travel times, or spatial extent) remains a challenge, particularly on larger scales. A number of different experimental quantification techniques exist, including heat tracing (Ren et al., 2019), conservative-tracer tests (Mallard et al., 2014), isotope-data interpretation (Zhang et al., 2017), differential river-discharge measurements (Kalbus et al., 2006), geophysical exploration (Ward et al., 2010), or seepage-meter applications (Langhoff et al., 2006). Each of these methods comes with its own strengths and limitations (see Cook, 2015, for a detailed comparison). Flow models represent an attractive addition to field experiments for the quantification of hyporheic exchange, because they are comparably cheap, versatile and allow full control over the respective system. Consequently, there is a long history of surface-water/groundwater exchange modeling studies, of which we want to highlight the ones most significant to our investigations.

1.2. Previous Work & Knowledge Gap

An early two-dimensional model of vertical hyporheic exchange was developed by Vaux (1968), who used electric analogs to visualize his findings, as neither a closed-form solution nor a numerical approximation

of his formulation were available/feasible at that time. Lateral hyporheic flow was modeled by Harvey and Bencala (1993), who applied the finite difference method to analyze the effect of alluvial streambed topography on hyporheic exchange in horizontal, rectangular domains. Revelli et al. (2008) used a finite volume model to evaluate lateral hyporheic exchange occurring within a river meander. Similarly, Cardenas (2009a, 2009b) developed finite element models to investigate hyporheic exchange between meanders in horizontal domains, incorporating also ambient river gain or loss. Huang and Chui (2018) derived proxy-equations for pool-riffle systems, serving as simplified empirical models to estimate the spatial scale of a hyporheic zone, as well as the related exchange flux and the median travel time of water flowing through it. Boyraz and Kazezyılmaz-Alhan (2013, 2017) developed (semi-)analytical solutions for two-dimensional flow in closed, horizontal, rectangular domains. As the only source and sink of groundwater in their cases is the simulated river, their studies can be interpreted as hyporheic flow investigations (where all water in the system belongs to the hyporheic exchange zone by definition). Recently, they expanded their work by deriving an analytical solution for hyporheic exchange in rectangular systems under the influence of groundwater recharge from ponds and wetlands (Boyraz & Kazezyılmaz-Alhan, 2021). In summary, many of these models have targeted hyporheic exchange for various settings, including the case (a) of Figure 1. However, we see a lack of research studying valley-scale lateral hyporheic exchange driven by the geometry of the floodplain aquifers (i.e., the case of spot (b) in Figure 1), which we want to address. To this end, we define an idealized two-dimensional plan-view model and solve it semi-analytically.

1.3. Semi-Analytical Methods

Within the modeling spectrum, semi-analytical techniques are located between fully analytical closed-form solutions and numerical methods. While fully analytical solutions are mathematically elegant, absolutely correct, scale- and discretization-independent, and very quick to evaluate, they are typically restricted to mostly inflexible simplistic problems with predefined geometries (e.g., rectangular domains) or simplistic boundary conditions (like the sinusoidal head fluctuations of Tóth, 1963). Numerical solutions, by contrast, can be used for problems of arbitrary complexity allowing full flexibility, but come at the cost of larger evaluation times and accuracy limitations often related to spatial (or temporal) discretization. In addition to that, spatially resolved models often require many parameters and input information that might not be available for all cases (see for example, Barthel & Banzhaf, 2016; Dall'O' et al., 2001). Semi-analytical methods represent a compromise between the two end members, as they are typically based on a set of simplifying assumptions, while maintaining the desired flexibility (e.g., by allowing arbitrary geometries or boundary condition values for relevant parts of the domain). This results in exact analytical expressions, which cannot directly be evaluated, for example, because they involve integrals without a general closed-form solution or infinite series with a set of coefficients that are fully determined but cannot be backed out (e.g., Zlotnik et al., 2011). Semi-analytical solutions solve these integrals or infinite-series coefficients by numerical methods. Once the set of approximate coefficients has been evaluated for a specific model setup, the semi-analytical expression can be used to evaluate the solution at the same convenience as a fully analytical solution. Semi-analytical techniques have been used in past hydrogeological research, in particular for vertical cross-sections of hillslopes connected to rivers, drainage ditches or groundwater bodies (e.g., Craig, 2008; Li et al., 1996; Powers, 1966; Read, 2007), but also for lateral two-dimensional problems (e.g., Boano et al., 2006; Gomez-Velez et al., 2017; Suribhatla et al., 2004). The Analytical Element Method (e.g., Bakker, 1999, 2006; Bakker & Strack, 2003; Fitts, 2010; O. D. Strack, 1989; O. D. L. Strack, 2003, 2018; O. D. L. Strack & Nevison, 2015) represents a large class of semi-analytical models. It allows the construction of solutions for a given problem with a modular superposition approach, where each internal or external boundary condition represents a so-called *analytical element*.

1.4. Objectives of This Study

In this study, we develop a semi-analytical solution for the valley-scale lateral hyporheic-exchange zone driven by the geometry of floodplain aquifers. We aim to answer three questions that are typically of interest when investigating hyporheic exchange (e.g., Huang & Chui, 2018; Kasahara & Wondzell, 2003; Welch et al., 2015), which address relevant aspects of biogeochemical reactive processes related to river-borne dissolved compounds:

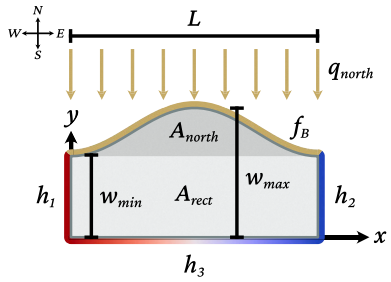

Figure 2. Schematic illustration of the two-dimensional problem definition. The tan line in the north represents a Neumann boundary with constant flux q_{north}. The other three lateral sides reflect Dirichlet boundaries with values h_1, h_2 and $h_3(x)$ (warmer colors indicate higher hydraulic heads). L, w_{min} and w_{max} represent the length of the domain as well as its minimum and maximum width. The shape of the northern boundary is defined by $f_B(x)$, which creates an additional area A_{north} compared to the rectangular area A_{rect}.

1. How much water (in terms of the volumetric flux) flows through the valley-scale lateral hyporheic exchange zone?

Answering this question allows comparing the exchange flux with the total river discharge and with total groundwater fluxes. If, for example, only a small fraction of the total river flow makes it into the aquifer, the river-water composition will not be drastically affected by the hyporheic exchange.

2. What is the spatial extent of the valley-scale lateral hyporheic zone?

This is important whenever field studies within the aquifer are conducted, because it marks the boundary of "true" groundwater and infiltrated river water, which might carry a different chemical signature (e.g., micropollutants originating from waste-water effluents).

3. How long does the river water stay in the valley-scale lateral hyporheic exchange zone before returning to the river?

The travel times quantify the contact time between water and aquifer material, which typically determines the degree to which any kinetic reactions or microbial interaction can take place.

After deriving the semi-analytical expression for an idealized two-dimensional floodplain aquifer, we perform a systematic parameter-variation study, to infer how the lateral exchange flux depends on the geometric and hydraulic input parameters. This allows us to construct approximate predictive proxy-models. We demonstrate the applicability of these proxy-models with two examples mimicking field sites close to Tübingen.

A comparable proxy-model for hyporheic exchange fluxes between sinuous river meanders has been developed by Cardenas (2009a, 2009b). Of course, each floodplain site is unique with all its complex three-dimensional geology, morphology and heterogeneity as well as its dynamic processes taking place on multiple scales. It is therefore certainly not possible to capture all details of a site with our simplified model, but it can give an easy and a quick order-of-magnitude type of estimation for the hyporheic-zone metrics of interest in cases where only little information about the floodplain is known (this motivation is similar to the one of Huang & Chui, 2018). Finally, our study gives insight into major dependencies, which might get lost in the details of a site-specific modeling study.

2. Methods

2.1. Conceptual Model/Problem Statement

We simulate steady-state horizontal groundwater flow in a simplified two-dimensional aquifer (see schematic illustration in Figure 2) without internal sources or sinks. The overall geometry idealizes the mid-section subcatchment of a typical channelized river in a landscape formed on bedrocks of alternating competence. In such settings, the large-scale along-valley ambient hydraulic gradient and the topography (including aquifer bottom and top) essentially follow the slope of the river, whereas the across-valley slopes are negligible. Laterally connected hillslopes are not part of our modeling domain; their effect on the floodplain aquifer are considered as boundary condition. The restriction to two dimensions can be justified by the typical large lateral extent of floodplain aquifers compared to their small and mostly uniform thickness (e.g., Clément et al., 2003). For ease of description, we will use the terms *northern* (in the direction of y), *eastern* (in the direction of x), *southern* (against the direction of y) and *western* (against the direction of x) to denote the four directions and boundaries.

The domain extends laterally within $0 \le x \le L$ and $0 \le y \le f_B(x)$. Here, L [L] represents the domain length. The continuous and real-valued function $f_B(x)$ defines the location of the northern boundary and thereby the domain width. At this northern end, a fixed specific flux $q_{\text{north}}(x)$ [$\text{L}^3/\text{L}/\text{T}$] crosses the boundary in y-direction, which simulates lateral inflow of an adjacent hillslope ($q_{\text{north}} < 0$ implies an influx). In the following derivations, we do not impose any further assumption or restriction with respect to $f_B(x)$, but in the

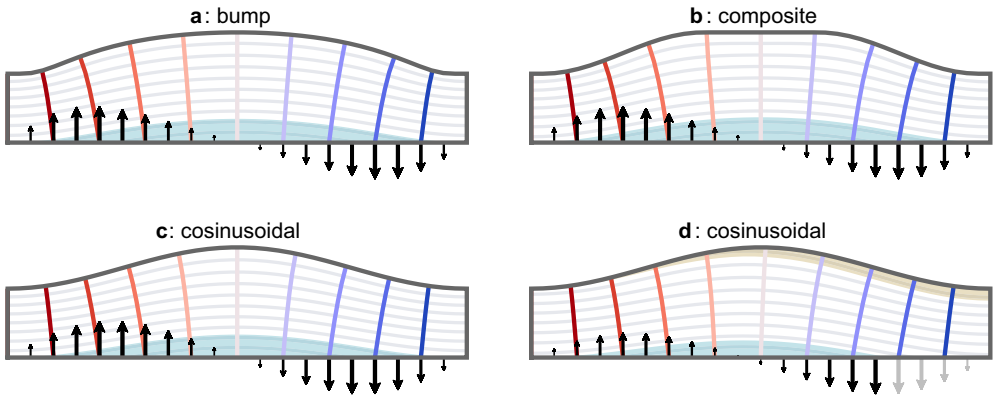

Figure 3. Four flow-net examples with colored head contour lines, gray stream function contour lines, and arrow indicators of exchange flux (black arrows highlight fluxes that occur within the hyporheic exchange zone). The hyporheic exchange zone is shown in blue, the zone of water originating from the northern boundary is shown in tan. (a–c) different shapes without northern influx; (d) with northern influx. The flow nets and flux indicators visualize actual results obtained with the semi-analytical solution.

investigated cases we will focus on a "cosinusoidal" curve mimicking the widening shape of a floodplain aquifer:

$$f_B(x) = w_{\min} + \frac{1}{2}(w_{\max} - w_{\min}) \cdot \left(1 - \cos\left(2\pi \frac{x}{L}\right)\right), \tag{1}$$

where $w_{\min}$ [L] is the minimum width of the domain (which applies for the western and eastern end) and $w_{\max}$ [L] is the maximum width (which occurs at $x = \frac{L}{2}$). In later comparisons, we also investigate two alternate shapes that we denote "composite" and "bump." The latter shape follows a classical bump function defined by the points $(0|w_{\min})$, $(\frac{L}{2}|w_{\max})$ and $(L|w_{\min})$ and uses the following equation:

$$f_B(x) = w_{\min} + (w_{\max} - w_{\min}) \cdot \exp\left(1 - \frac{1}{1 - \left(\frac{2x}{L} - 1\right)^2}\right). \tag{2}$$

The "composite" configuration is defined as a piece-wise function by connecting the six points $(0|w_{\min})$, $(p_1|w_{\min})$, $(p_2|w_{\max})$, $(p_3|w_{\max})$, $(p_4|w_{\min})$ and $(L|w_{\min})$ with three constant and two cosinusoidal segments to achieve an elongated shape with continuous first derivative. We use the following equation:

$$f_B(x) = \begin{cases} w_{\min} & ; \frac{x}{L} < p_1 \\ w_{\min} + \frac{1}{2}(w_{\max} - w_{\min})\left(1 - \cos\left(\pi \frac{x - p_1}{p_2 - p_1}\right)\right) & ; p_1 \le \frac{x}{L} < p_2 \\ w_{\max} & ; p_2 \le \frac{x}{L} < p_3, \\ w_{\min} + \frac{1}{2}(w_{\max} - w_{\min})\left(1 + \cos\left(\pi \frac{x - p_3}{p_4 - p_3}\right)\right) & ; p_3 \le \frac{x}{L} < p_4 \\ w_{\min} & ; p_4 \le \frac{x}{L} \end{cases} \tag{3}$$

with the four parameters $p_1 = \frac{1}{40}$, $p_2 = \frac{15}{40}$, $p_3 = \frac{25}{40}$ and $p_4 = \frac{39}{40}$. These parameters create a straight central section of length $\frac{L}{2}$ and straight inlet and outlet sections with a total length of a tenth of that.

Figure 3 shows example geometries for all three domain shapes. We denote the rectangular area of the southern part A_{rect} [L^2] and the additional northern area A_{north} [L^2], such that the total surface area of the domain A_{tot} [L^2] is the sum of the two:

$$A_{\text{tot}} = A_{\text{rect}} + A_{\text{north}} = L \cdot w_{\text{min}} + A_{\text{north}}. \tag{4}$$

At the western and eastern boundaries, the fixed heads h_1 [L] (western boundary) and h_2 [L] (eastern boundary) impose an ambient flow field, which we assume to be connected to adjacent aquifers up- and downstream of the investigated catchment segment. The southern boundary is assumed to be in perfect hydraulic contact with a river that provides another fixed-head boundary with $h_3(x)$ linearly varying between h_2 and h_1. We allow the hydraulic conductivity to be anisotropic in the principal directions (x and y), leading to a diagonal transmissivity tensor $\mathbf{T}$ [L^2/T]:

$$\mathbf{T} = \begin{pmatrix} T_x & 0 \\ 0 & T_y \end{pmatrix}. \tag{5}$$

The evaluation of travel times requires a depth-integrated flow-effective porosity, or the aquifer thickness times the mean porosity, which we denote Φ [L].

2.2. Semi-Analytical Solution for Hydraulic Head and Stream Function

The starting point of our derivation is the two-dimensional, steady-state, anisotropic groundwater-flow equation for divergence-free flow. It involves the hydraulic head h, the spatial coordinates x and y and the transmissivities T_x and T_y (e.g., Bear, 1972):

$$\frac{\partial^2 h}{\partial x^2} + \frac{T_y}{T_x}\frac{\partial^2 h}{\partial y^2} = 0. \tag{6}$$

The Cauchy-Riemann equations (e.g., Bear, 1972; O. D. L. Strack, 2017):

$$\frac{\partial \Psi}{\partial x} = T_y \frac{\partial h}{\partial y} \tag{7}$$

$$\frac{\partial \Psi}{\partial y} = -T_x \frac{\partial h}{\partial x}, \tag{8}$$

relate the hydraulic head with the stream function Ψ [L^3/T]. The stream function helps in formulating Neumann ("fixed flux") boundaries and allows for trivial flux evaluations after obtaining its solution.

We want to find the solution $h(x, y)$ of Equation 6 meeting the following boundary conditions:

$$h = h_1 \quad \text{at } x = 0 \tag{9}$$

$$h = h_2 \quad \text{at } x = L \tag{10}$$

$$h = h_1 + \frac{h_2 - h_1}{L} x \quad \text{at } y = 0 \tag{11}$$

$$-(\mathbf{T}\nabla h) \cdot \mathbf{n}(x) = \frac{1}{\sqrt{f_B'(x)^2 + 1}} q_{\text{north}}(x) \quad \text{at } y = f_B(x), \tag{12}$$

where $\mathbf{n}(x)$ is the unit normal vector along the northern boundary (pointing outwards) and $f_B'(x)$ is the derivative of $f_B(x)$ in the x-direction. Similar to the derivation of Read (2007), it is possible to express the northern Neumann boundary in terms of the stream function, such that Equations 12 and 13 are equivalent (see Text S1):

$$\Psi(x, f_B(x)) = -\int q_{\text{north}}(\xi)\,\mathrm{d}\xi = R(x) \quad \text{at } y = f_B(x). \tag{13}$$

Note that the stream function is only defined subject to an arbitrary constant offset. Like in most studies, we are only interested in differences between stream-function values so that the offset drops out. To clarify dimensions: $q_{\text{north}}(x)$ is a (potentially location-dependent) specific flux expressed in L^2/T and $R(x)$ represents a fixed value for the stream function and is therefore expressed in L^3/T.

By separation of variables (a detailed derivation is given in Text S2) we derive the following series solution of the boundary-value problem:

$$h(x, y) = h_1 + \frac{h_2 - h_1}{L} \cdot x + \sum_{n=1}^{\infty} A_n \sin\left(\frac{n \cdot \pi}{L} x\right) \sinh\left(\frac{n \cdot \pi}{L} \kappa y\right), \tag{14}$$

where A_n [L] is the n-th series coefficient and κ represents the dimensionless square root of the anisotropy ratio $\kappa = \sqrt{\frac{T_x}{T_y}}$. The associated stream function is:

$$\Psi(x, y) = -T_x \cdot \left(A_0 + \frac{h_2 - h_1}{L} \cdot y + \frac{1}{\kappa} \sum_{n=1}^{\infty} A_n \cos\left(\frac{n \cdot \pi}{L} x\right) \cosh\left(\frac{n \cdot \pi}{L} \kappa y\right) \right), \tag{15}$$

in which the coefficient A_0 [L] reflects the arbitrary offset of the stream function.

The series coefficients $\mathbf{A}$ (i.e., A_0 to A_n) are fully determined by the shape of the northern boundary $f_B(x)$ and the associated boundary condition $R(x)$:

$$-T_x \cdot \left(A_0 + \frac{h_2 - h_1}{L} \cdot f_B(x) + \frac{1}{\kappa} \sum_{n=1}^{\infty} A_n \cos\left(\frac{n \cdot \pi}{L} x\right) \cosh\left(\frac{n \cdot \pi}{L} \kappa f_B(x)\right) \right) \overset{!}{=} R(x). \tag{16}$$

However, except for very simple cases (e.g., a valley with uniform width and constant normal flux at the northern boundary) it is practically impossible to determine the coefficients analytically. We alleviate this problem by numerical approximations of the series with a finite number of terms. We use an approach similar to the analytical element method of O. D. Strack (1989), that was refined and applied by Barnes and Janković (1999), Janković and Barnes (1999), Read (2007) and Craig (2008). In essence, we choose a finite number of M points along the northern boundary $(x_i | f_B(x_i))$, that are used to evaluate the $N + 1 \leq M$ coefficients $\mathbf{A}$, in which N is the number of terms in the truncated infinite series.

The solution of Equation 16 can then be obtained through a least squares formulation minimizing the sum of squared approximation errors ε along the northern boundary:

$$\varepsilon_i(\mathbf{A}) = A_0 + \sum_{n=1}^{\infty} A_n f_n(x_i) - g(x_i), \tag{17}$$

with

$$g(x_i) = -\frac{R(x_i)}{T_x} - \frac{h_2 - h_1}{L} \cdot f_B(x_i), \tag{18}$$

and

$$f_n(x_i) = \frac{1}{\kappa} \cos\left(\frac{n \cdot \pi}{L} x_i\right) \cosh\left(\frac{n \cdot \pi}{L} \kappa f_B(x_i)\right). \tag{19}$$

The goal is to minimize the sum of (potentially weighted) squared approximation errors across the M points:

$$\hat{\mathbf{A}} = \arg\min_{\mathbf{A}} \sum_{i=1}^{M} w_i \cdot \varepsilon_i(\mathbf{A})^2, \tag{20}$$

in which w_i represents the weight of the i-th point. This optimization problem is converted to a system of linear equations by setting the derivative to zero (Craig, 2008). This yields $N + 1$ equations with $N + 1$ unknowns, regardless of the number of points M:

$$A_0 \sum_{i=1}^{M} w_i \cdot f_\eta(x_i) + \sum_{n=1}^{N} A_n \cdot \sum_{i=1}^{M} w_i f_\eta(x_i) f_n(x_i) = \sum_{i=1}^{M} w_i f_\eta(x_i) \cdot g(x_i); \quad \eta = 1 \ldots N, \tag{21}$$

$$A_0 + \sum_{n=1}^{N} A_n \cdot \sum_{i=1}^{M} w_i f_n(x_i) = \sum_{i=1}^{M} w_i \cdot g(x_i). \tag{22}$$

In the case of $M = N + 1$, the system is determined and the solution will be met exactly on all M points. Then, these points are referred to as *collocation points* (Barnes & Janković, 1999). Unfortunately, the Gibbs-Wilbraham (Gibbs, 1898; Wilbraham, 1848) and Runge phenomena (Runge, 1901) can lead to significant and strong oscillations between the points, which cannot be fixed by increasing the approximation order N (for more information see for example, Hewitt & Hewitt, 1979; Ray, 2020; Read, 2007). Instead, it can be beneficial to choose more points than coefficients to reduce the adverse effects of the Gibbs-Wilbraham phenomenon. The resulting solution will then not be met exactly at all points (the system of equations is over-determined), but the error is minimized in an average sense. In such a case of $N + 1 < M$ the points are typically called *control points* (Barnes & Janković, 1999). In our study, we use $N = 10$ and $M = 25$.

As highlighted by Craig (2008), additional Gibbs-Wilbraham effects can be caused wherever Dirichlet and Neumann boundaries meet at angles that lead to inconsistent hydraulic gradients. In our model setup this can happen at the intersection points of the northern boundary and the western and eastern boundaries, depending on the choice of $f_B(x)$ and $q_{\text{north}}(x)$. In problematic cases, according to Craig (2008), non-uniform weights with smaller values close to these points can reduce the influence of these inconsistencies on the remaining parts of the domain. Another way to deal with the problem is to use a non-uniform spacing of the points x_i. Neither of these remedies were necessary in this study, so that we used identical weights for all points x_i spaced equidistantly (tests with parameter combinations outside of the investigated ranges suggest that the most critical parameters with respect to the Gibbs-Wilbraham phenomenon are strong anisotropies and extreme width-to-length ratios).

The system of equations that we solve includes hyperbolic cosine terms (see Equations 19, 21 and 22). As the hyperbolic cosine function grows rapidly with its argument, it can be useful to reformulate the solution to avoid terms that grow exponentially with n. This is possible by redefining the series coefficients A_1 to A_n and scaling them with a hyperbolic cosine term to obtain:

$$A_n^* = A_n \cdot \cosh\left(\frac{n\pi}{L} \kappa w_{\max}\right), \tag{23}$$

in which A_n^* [L] are the modified series coefficients and $w_{\max}$ is the maximum extent of the northern boundary. The resulting ratios of hyperbolic sine and cosine functions can be exploited with the identities:

$$\frac{\sinh(t)}{\cosh(b)} = \frac{\exp(t-b) - \exp(-t-b)}{1 + \exp(-2b)}, \tag{24}$$

and

$$\frac{\cosh(t)}{\cosh(b)} = \frac{\exp(t-b) + \exp(-t-b)}{1 + \exp(-2b)}, \tag{25}$$

that involve only terms having a negative sign in the exponential for our case. This results in modified versions of the hydraulic head function:

$$h(x,y) = h_1 + \frac{h_2 - h_1}{L} \cdot x + \sum_{n=1}^{\infty} A_n^* \sin(cx) \frac{\exp(c\kappa(y - w_{\max})) - \exp(-c\kappa(y + w_{\max}))}{1 + \exp(-2c\kappa w_{\max})}, \tag{26}$$

and the stream function:

$$\Psi(x,y) = -T_x \cdot \ldots \left(A_0 + \frac{h_2 - h_1}{L} \cdot y + \frac{1}{\kappa} \sum_{n=1}^{\infty} A_n^* \cos(cx) \frac{\exp(c\kappa(y - w_{\max})) + \exp(-c\kappa(y + w_{\max}))}{1 + \exp(-2c\kappa w_{\max})} \right), \tag{27}$$

which make use of a new shorthand $c = \frac{n\pi}{L}$. A similar procedure has been exploited by Powers (1966) and Powers et al. (1967). If there was an ideal computer with infinite precision the solutions of the two

formulations were identical, and the only difference would lie in the magnitude of the series coefficients. Due to round-off errors, however, the modified version yields more precise results when using standard double precision floating-point operations.

2.3. Characterization of the Hyporheic-Exchange Zone

Figure 3 shows semi-analytical flow nets for different model configurations, as well as directions and magnitudes of the flux perpendicular to the southern boundary. This flux is zero at the western end ($x = 0$). Depending on the geometric configuration and the northern influx rate, it typically increases with x until it reaches a maximum. From there on, it decreases again, passes zero and becomes negative until it reaches a minimum. Finally, it increases again to reach zero once more at the eastern end ($x = L$). In summary, we can observe in the western part a net flux from the river to the aquifer and a reversed flux in the eastern part. Without a northern influx the pattern is symmetric and the net exchange between the river and the aquifer is zero. By following the stream lines, we can identify the parts of the domain, where the flow originates from the river and returns to it again. These parts define the valley-scale hyporheic exchange zone (blue areas in Figure 3). In the following we derive how to quantify the flux of water flowing through this zone (the hyporheic-exchange flux Q_{ex}), how large the hyporheic exchange zone is (the exchange zone area A_{ex}) and how travel times through this zone are distributed.

2.3.1. Exchange Flux

As exchange flux, we define the discharge (in L^3/T) of water originating from the river at the southern boundary and returning back to it again. We can quantify the exchange flux by considering the stream function, which is defined such that the net discharge Q_{pq} crossing a line between two points p and q equals the absolute difference of the stream-function values at the two end points:

$$Q_{\mathrm{pq}} = \left|\Psi(x_q, y_q) - \Psi(x_p, y_p)\right|. \tag{28}$$

In Figure 3 we can see different manifestations of the exchange zone. It can span the entire southern boundary (see Figures 3a, 3b and 3c), parts of it (see Figure 3d) or may vanish completely (e.g., if the northern influx is very large). In any case, however, it is bounded by a dividing streamline that starts and/or ends at one of the southern corner points of the domain (i.e., either (0|0) or (L|0)). According to Equation 7, an increase in the stream-function value along the southern boundary in the positive x-direction implies an exfiltration flux (groundwater discharge to the river). Thus, in the cases shown in Figure 3, the stream-function first decreases along the southern boundary, reaches a minimum and increases back until it reaches its initial value. In the case of Figure 3d it further increases, because the river gains more water than it loses. In this setting, the exchange flux is given by the stream-function values at (0|0) and at the minimum point. With different geometries (e.g., a valley that first gets narrower and then widens) the southern boundary may start with exfiltrating conditions (river gaining groundwater). In that case the exchange flux is given by the difference of the stream-function values at the end point (L|0) and at the minimum, such that all cases are covered by:

$$Q_{\mathrm{ex}} = \min[\Psi(0,0), \Psi(L,0)] - \min[\Psi(x,0)]. \tag{29}$$

If there is no hyporheic-exchange zone, the end point with the smaller stream-function value is identical with the point of minimal stream-function value, leading to the correct exchange flux of zero. In general, the minimum of the stream function along the southern boundary $\min(\Psi(x,0))$ must be evaluated numerically. If the number M of points to determine the coefficients $\mathbf{A}$ was large enough, it is convenient to re-use the same set of x-locations that were also selected for constructing the system of equations.

2.3.2. Area of the Exchange Zone

The volume V_{ex} of the exchange zone can be expressed in terms of a two-dimensional area:

$$A_{\mathrm{ex}} = \frac{V_{\mathrm{ex}}}{\Phi}, \tag{30}$$

where we make use of the depth-integrated effective porosity Φ. Just as for the calculation of the exchange flux, a general analytical solution for the area of the exchange zone is not available. Hence, we determine the area numerically by constructing a polygon bounded by the southern domain border and the dividing streamline separating the exchange zone from the northern rest of the domain. The dividing streamline is the contour line of Ψ representing a value of $\min[\Psi(0,0),\Psi(L,0)]$. It can be constructed with standard contouring algorithms from a set of point observations of $\Psi(x,y)$ placed throughout the domain. The evaluation of the polygonal area is trivial; we only need to make sure that we use enough points to approximate the polygon well enough. Again, it might be convenient to reuse the set of x-nodes in combination with a set of y-nodes for the construction of a mesh of points where Ψ is evaluated.

2.3.3. Travel Time Distribution

The mean travel time of water flowing through the hyporheic exchange zone is given by the ratio of its volume and the exchange flux:

$$t_{\text{mean}} = \frac{V_{\text{ex}}}{Q_{\text{ex}}} = \frac{\Phi A_{\text{ex}}}{Q_{\text{ex}}}. \tag{31}$$

In order to evaluate the full travel-time distribution of all water parcels flowing through the exchange zone we construct n_t contour lines of Ψ across the full range of Ψ-values within the exchange zone (i.e., from $\min[\Psi(x,0)]$ to $\min[\Psi(0,0),\Psi(L,0)]$). By choosing equal steps between the contour line values (i.e., a constant $\Delta\Psi$), we construct stream-tubes of identical discharge. For each contour line we determine the respective travel time t [T] and the fraction $F(t)$ of discharge that has a travel time smaller than t. This gives one point of the travel-time distribution per contour line.

The travel time t_i of the i-th contour line can be approximated by summation of the travel times t_{seg} of all its n_{seg} line segments. A segment's travel time can be determined from its length L_{seg} and its average flow velocity v_{avg}. We assume that the velocities of the segment endpoints (v_1 and v_2) apply both each for half of the segment length, which results in an arithmetic averaging procedure:

$$t_i = \sum_{j=1}^{n_{\text{seg}}} t_{\text{seg}} = \sum_{j=1}^{n_{\text{seg}}} \frac{L_{\text{seg}}}{\mathbf{v}_{\text{avg}}} = \sum_{j=1}^{n_{\text{seg}}} \frac{2 \cdot L_{\text{seg}}}{|\mathbf{v}_1| + |\mathbf{v}_2|}. \tag{32}$$

Here, the linear velocity $\mathbf{v}$ [L / T] is given by Darcy's law (Darcy, 1856) and the depth-integrated porosity Φ:

$$\mathbf{v} = -\frac{1}{\Phi}\mathbf{T}\nabla h. \tag{33}$$

The corresponding fraction of hyporheic discharge that has a travel time smaller than t_i can be determined with the stream function:

$$F(t_i) = \frac{\Psi_i - \min(\Psi(x,0))}{Q_{\text{ex}}}, \tag{34}$$

where Ψ_i is the stream function value of the i-th contour line. The n_t points $(t_i | F(t_i))$ describe the approximated cumulative distribution function of travel time. For better comparison among different settings, we normalize the travel-time distribution by the mean travel time, which yields a dimensionless time:

$$\tilde{t} = \frac{t}{t_{\text{mean}}}. \tag{35}$$

Table 1
Constant Hydraulic Parameter Values for Analyzing the Effects of Geometric Properties on Hyporheic-Exchange Metrics

Parameter	Symbol	Value	Unit
Fixed head at inlet	h_1	3	m
Fixed head at outlet	h_2	0	m
Transmissivity in x	T_x	10^{-3}	m^2/s
Transmissivity in y	T_y	10^{-3}	m^2/s
Northern influx	q_{north}	0	m^2/s

2.3.4. Summary of the Semi-Analytical Procedure

In short, the semi-analytical determination of hyporheic-exchange-zone properties for a given setting involves the following steps:

1. Define all parameter values (including those describing the geometry).
2. Decide on N, M and x_i.

3. Set up the system of equations (Equations 21 and 22).
4. Solve the system of equations to obtain the coefficients $\mathbf{A}$.
5. Evaluate the stream function on selected points to determine Q_{ex}, A_{ex} or $F(t)$ according to Equations 29, 30 and 34.

Depending on N and M, this scheme can be computationally expensive. Also, it gives no direct evidence of how parameters affect the exchange flux, the area of the exchange zone, or the travel-time distribution. As our primary interest is to relate these quantities to the various input parameters, we perform a systematic parameter-variation study setting the base for easy-to-use empirical relationships.

3. Relating Exchange-Zone Metrics to Hydrogeological and Geometric Properties of the Floodplain Aquifer

As first target of the parameter-variation study we consider the hyporheic-exchange flux, before addressing the hyporheic-zone area and the travel-time distribution.

3.1. Exchange Flux

We focus on the "cosinusoidal" shape to infer relationships between the input parameters and Q_{ex} and use the "bump" and "composite" shapes for verifying the derived expression. For the interested reader, we also provide a global sensitivity analysis of Q_{ex} using Sobol indices (Sobol', 1993, 2001) in Text S3.

3.1.1. Cosinusoidal Shape

To understand how the hyporheic-exchange flux relates to the domain geometry for a given hydraulic set-up, we fix all hydraulic parameters to the values defined in Table 1 and vary the domain length in the range $500\text{m} \leq L \leq 3500\text{m}$, the minimum width in the range $50\text{m} \leq w_{min} \leq 350\text{m}$ and the ratio of maximum to minimum width in the range $1.0 \leq \frac{w_{max}}{w_{min}} \leq 2.5$. With this initial sample, we can resemble most of the floodplain examples mentioned previously, which range from a few hundred meters to a few kilometers in length and have approximate w_{max}/L ratios between 10% and 50% (e.g., Clément et al., 2003; Ó Dochar-

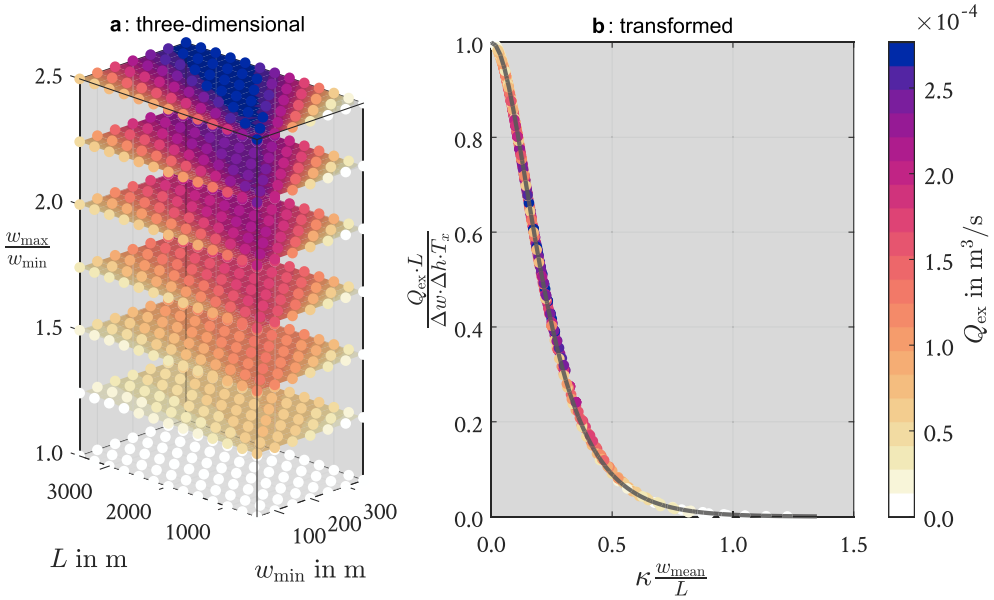

Figure 4. Response of the exchange flux to geometric parameters; (a) slices and scatter plot involving geometric parameters; (b) transformation bringing the response of the exchange flux to all three geometric parameters onto a single curve that can be approximated by a scaled hyperbolic secant function (black line).

taigh et al., 2019) and approximate w_{max}/w_{min} ratios of up to 2.5 (e.g., Castro & Hornberger, 1991; Helton et al., 2012).

Figure 4a shows a three-dimensional slice and scatter plot of corresponding exchange fluxes for the $13 \times 7 \times 7 = 637$ parameter combinations that we tested.

This plot reveals the following insights: (a) For a width ratio of one, the exchange flux is zero, independent of the other two parameters. This is obvious, because the domain collapses to a rectangle, where the solution of the related system of equations is trivial (A_1 to A_n equal zero) and there is no driving force for any lateral hyporheic exchange. (b) For a fixed length and minimum width, the exchange flux increases monotonically with the ratio of w_{max} to w_{min}. (c) For any fixed width-ratio larger than one, the magnitude of the exchange flux depends on both the domain length and the minimum width. (d) There seems to be a ratio of the latter two that gives a maximum flux. (e) For ratios larger or smaller than that, the exchange flux declines.

This rather complex behavior in three-dimensional parameter space can be simplified and the dimensionality can be reduced. Figure 4b shows that all simulated points can be brought very close to a single curve by plotting the following two transformed quantities against each other: On the horizontal axis we display the ratio of the average width to the domain length. For that we calculate the average domain width by dividing the domain's total area by its length:

$$w_{mean} = \frac{A_{tot}}{L}. \tag{36}$$

On the vertical axis of the transformed plot, we show the product of the exchange flux and the ratio of domain length to the transmissivity in x-direction and maximum width-difference Δw, which is:

$$\Delta w = w_{max} - w_{min}. \tag{37}$$

After subsequent variations of the hydraulic properties h_1, h_2 and κ for fixed geometries (not shown), we found an easy way to incorporate their influence on the exchange flux into the existing transformation as long as there is no northern hillslope influx (i.e., $q_{north} = 0$): The square root of the anisotropy ratio κ affects only the scaling in the direction of the horizontal axis and needs to be multiplied with the ratio of the average width to the domain length. The hydraulic heads h_1 and h_2 only matter as a head difference:

$$\Delta h = h_1 - h_2. \tag{38}$$

This difference only affects the vertical axis of the plot and can be accounted for in dividing the existing expression by Δh.

The one-dimensional relationship derived in this way (see Figure 4b) starts at the point (0|1) and is characterized by a monotonic decline that has a small slope in the beginning, a steeper part around 0.25 and a tail asymptotically approaching zero. Such a behavior can be approximated by a hyperbolic secant function scaled in the direction of the horizontal axis (Figure 4b contains such a function fitted to the simulated model results). This relationship can be inverted to a description of the dimensional hyporheic-exchange flux depending on all model parameters (with exception of q_{north}, which has been set to zero so far). As a result, we postulate the approximation:

$$Q_{ex} \approx Q_0 \cdot \operatorname{sech}\left(a_1 \cdot \kappa \frac{w_{mean}}{L}\right), \tag{39}$$

with a dimensionless fitting parameter a_1 and the reference discharge:

$$Q_0 = I_x \cdot T_x \cdot \Delta w = \frac{h_1 - h_2}{L} \cdot T_x \cdot (w_{max} - w_{min}), \tag{40}$$

where I_x is the ambient hydraulic gradient in x-direction, which is given by the ratio of the head difference Δh to the domain length L.

We can interpret the relationship of Equation 39 in the following way: (a) The difference between the maximum and minimum width of the valley exerts a linear control on the hyporheic exchange flux. (b) For a given width difference, there is a maximum potential exchange flux Q_0. (c) The magnitude of this flux

linearly depends on the ambient hydraulic gradient and the hydraulic transmissivity in x-direction. (d) The actual exchange flux Q_{ex} is smaller than Q_0 and the ratio of the two is determined by the domain aspect ratio (w_{mean}/L) and the anisotropy ($\kappa = \sqrt{T_x/T_y}$). We explain the details of this relationship in the following.

To understand the equation for Q_0, it makes sense to analyze the illustrative extreme case of w_{min} approaching zero in a scenario of constant Δw. As seen in Figure 2, in such a case nearly the entire domain belongs to the northern part A_{north}, and A_{rect} becomes small. Basically all water flowing through the domain must come exclusively from the river and return to it again (i.e., $A_{tot} = A_{north} = A_{ex}$). The easiest way to quantify the exchange flux for this specific scenario is to take a look at the widest part of the domain (i.e., $x = \frac{1}{2}L$). Here, the discharge Q^* through the domain, is given by Darcy's law with the following approximation:

$$Q^* = \Delta w\left(-T_x \frac{\partial h}{\partial x}\right) \approx \Delta w \cdot T_x \frac{h_1 - h_2}{L}, \tag{41}$$

where we assume a uniform hydraulic gradient in x-direction equaling $-\Delta h$ over L. T_x is the only transmissivity that matters here, because the hydraulic gradient in the y-direction is zero. It becomes clear now, that Q^* equals our reference discharge Q_0 and it represents the maximum discharge that could be reached for a given Δw and adjustable w_{min}.

The actual exchange flux can be smaller than Q_0 for two reasons: first the curvature of the domain/flow-paths and second the distance between northern and southern boundary. Both of these effects are summarized in the term w_{mean}/L within the hyperbolic secant function in the following way: Even in cases with $w_{min} \to 0$, the actual exchange flux is smaller than Q_0, because of the curvature of the domain's northern boundary. This curvature leads to flow path lengths larger than L. Consequently, the hydraulic gradient $\partial h / \partial x$ is smaller than I_x at $x = \frac{L}{2}$. For given domain widths, L serves as a control to change the curvature, with $L \to \infty$ resulting in less curved flow-paths yielding $Q_{ex} \to Q_0$. In addition to that, the deviation of Q_{ex} from Q_0 depends on the average domain width w_{mean}, which is a measure for how far the northern boundary (i.e., the driving force) is separated from the river. As the hyperbolic secant function decreases strictly monotonically, a larger separation distance always leads to a decrease of hyporheic exchange flux. This is in line with intuition: if the northern valley expansion is far away from the river, the water necessary to "fill" A_{north} can be drawn from the western boundary without affecting the river too much (an illustrative example is given in Text S4).

The hydraulic anisotropy acts as a scaling factor for the average aspect ratio w_{mean}/L of the domain, meaning that if $T_y > T_x$, it becomes easier to draw water from the river, having the same effect as moving the northern boundary closer to it. Vice versa, a case of $T_x > T_y$ can be interpreted as increasing the distance between river and northern boundary. As κ represents the square root of the anisotropy ratio T_x/T_y, we can summarize the anisotropy-corrected aspect ratio to a new dimensionless variable:

$$\tilde{x} = \kappa \frac{w_{mean}}{L}, \tag{42}$$

which can be used to construct a dimensionless formulation for the exchange flux $\tilde{Q}_{ex}$:

$$\tilde{Q}_{ex} = \frac{Q_{ex}}{Q_0} \approx \operatorname{sech}\left(a_1 \cdot \tilde{x}\right). \tag{43}$$

In the following, we want to analyze the dependence of the hyporheic exchange flux on the northern hillslope influx q_{north} to generalize Equation 43. Toward this end, we normalize the total northern discharge by Q_0, to obtain the dimensionless quantity:

$$\tilde{Q}_{north} = \frac{\int_0^L q_{north}\, dx}{Q_0} = \frac{q_{north}}{T_x} \cdot \frac{L^2}{h_1 - h_2} \cdot \frac{1}{w_{max} - w_{min}}. \tag{44}$$

An influx from the northern boundary leads to a reduction of the hyporheic exchange flux, because the exchange zone is "pushed" toward the river boundary. At sufficiently large values of $\left|\tilde{Q}_{north}\right|$, the exchange zone may even vanish completely, meaning that no river-water infiltration takes place. By systematically varying

Table 2
Ranges of Geometric and Hydraulic Parameters That Were Explored in the Stochastic Simulation to Obtain Shape-Dependent Empirical Coefficients

Parameter	Symbol	Minimum	Maximum	Unit
Length	L	100.0	3000.0	m
Gradient	I_x	0.0	3.0	%
Length ratio	w_{max}/L	0.1	0.5	–
Width ratio	w_{max}/w_{min}	0.4	1.0	–
Log. transmissivity	$\log_{10}(\sqrt{T_x T_y})$	−6.0	−2.3	T in m^2/s
Log. anisotropy	$\log_{10}(T_x/T_y)$	−1.0	1.0	–
Northern influx	$\tilde{Q}_{north}$	−3.0	0.0	–

$\tilde{Q}_{north}$ in test cases (see Text S5), we found that the following nonlinear subtraction relationship matched the exchange flux across all tested parameter combinations best:

$$\tilde{Q}_{ex} \approx \operatorname{sech}(a_1\tilde{x}) \cdot \max\left[0{,}1 - a_2 \cdot \left|\tilde{Q}_{north}\right| \cosh(a_3\tilde{x})\right]. \tag{45}$$

This involves a second empirical function with two coefficients a_2 and a_3, employing the hyperbolic cosine function. The implementation of the maximum-value function constructs a threshold leading to a constant exchange flux of $\tilde{Q}_{ex} = 0$ in cases of large values of $|\tilde{Q}|_{north}$. This threshold can also be used to give a simple approximate logical expression indicating if the exchange zone is present for a given case of $\tilde{Q}_{north}$ and $\tilde{x}$:

$$1 > a_2 \left|\tilde{Q}_{north}\right| \cosh(a_3\tilde{x}). \tag{46}$$

In summary, our proxy-expression for the estimation of the hyporheic-exchange flux has a single empirical coefficient in case of zero northern influx, and two additional coefficients in cases with non-zero northern influx. We will determine and compare these coefficients in the following for different shapes of the floodplain.

3.1.2. Empirical Coefficients for Different Shapes

We construct a sample of 1,500 quasi-random model realizations to test whether the derived proxy-equation also works for shapes other than the "cosinusoidal" one. The parameter values of all realizations are drawn from uniform probability distributions within the ranges documented in Table 2, in which the sampling of parameter sets is done with a scrambled Halton sequence (Cheng & Druzdzel, 2013; Halton, 1960; Kocis & Whiten, 1997).

For each realization (i.e., parameter combination) we solve the semi-analytical model six times, twice for each of the three shapes ("cosinusoidal", "bump" and "composite"), with and without influx from the northern hillslope. This allows determining the empirical fitting coefficient a_1 independently of a_2 and a_3. Figure 5 shows the resulting normalized hyporheic-exchange flux for this stochastic model sample.

This figure could also be used as a tool to determine $\tilde{Q}_{ex}$ from $\tilde{x}$ and $|\tilde{Q}_{north}|$ graphically. Table 3 lists the fitted empirical coefficients and metrics indicating the quality of the fits.

The results are similar for all three shapes and closely follow the hyperbolic secant curve in the cases without northern influx. Considerable differences between the shapes only occur for large northern influxes, but are mostly restricted to how quickly the associated exchange flux drops. The "bump" and "composite" shape are very similar to each other and exhibit a slower decrease of $\tilde{Q}_{ex}$ with increasing $\tilde{Q}_{north}$ compared to

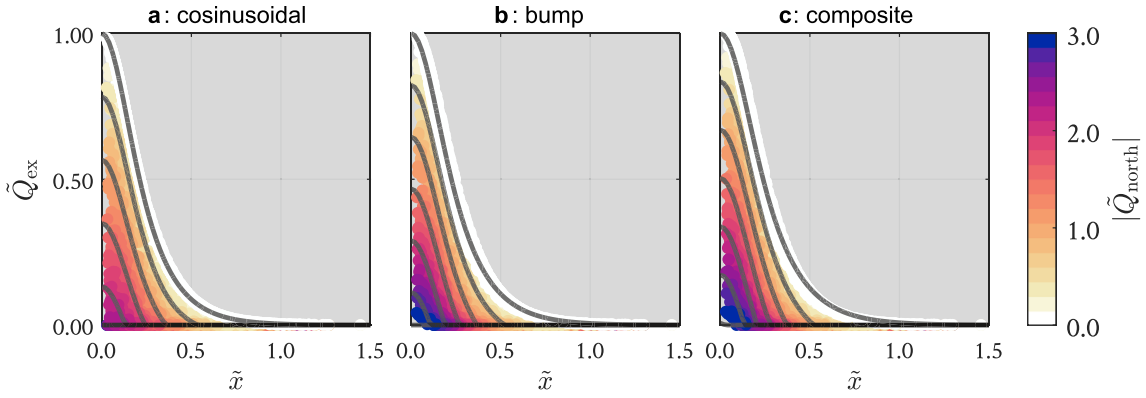

Figure 5. Dimensionless exchange flux results for three domain shapes with fitted proxy-models shown for different values of $|\tilde{Q}_{north}|$ (0.0, 0.5, 1.0, 1.5, 2.0, 2.5 and 3.0).

the "cosinusoidal" shape. The qualitative behavior, however, is identical for all domain shapes. This is also reflected in the fitted coefficients a_1, a_2, and a_3, which differ only slightly between the shapes.

We quantify the quality of the proxy-equation with the root-mean-square error of $\tilde{Q}_{ex}$ when comparing the proxy-equation to the semi-analytical solution. We do this independently for the cases, in which the northern influx is zero ("$RMSE_0$"), and those with a non-zero northern influx ("$RMSE_{\neq 0}$"). Given that $\tilde{Q}_{ex}$ ranges between zero and one, the RMSE-values of up to 0.027 indicate a very good agreement between the proxy-equation and semi-analytical solution and reveal that our interpretations are valid across the different domain shapes. Finally, we performed a linearized uncertainty propagation to estimate the uncertainties of the fitted coefficient values. The resulting relative uncertainties (shown in Table 3) are on the order of a few percent or less, indicating a high confidence in the fitted coefficients.

3.2. Area of the Exchange Zone

For each realization of the model sample, we determined the area of the hyporheic-exchange zone. In this section, we construct a simplified proxy-equation relating this area to the model input parameters. To do so, we define a dimensionless area $\tilde{A}$, by normalizing A_{ex} with A_{north} for all realizations. This dimensionless area seems to be approximately proportional to $\tilde{Q}_{ex}$, and additionally depends on $|\tilde{Q}_{north}|$ in the following nonlinear way:

$$\tilde{A} = \frac{A_{ex}}{A_{north}} \approx \frac{\tilde{Q}_{ex}}{\sqrt{1+|\tilde{Q}_{north}|}}. \tag{47}$$

Figure 6 shows that the 3,000 simulations decently follow this curve for all three domain shapes, and Table 4 summarizes the respective quality of the fits. Again, the RMSE values ($RMSE_{area}$) of up to 0.028 are small compared to the range of observed values (zero to one).

Table 3
Fitted Proxy-Model Coefficients and Quality of Fit Metrics for the Sample of 1,500 Model Realizations Per Domain Shape

Shape	a_1	a_2	a_3	$RMSE_0$	$RMSE_{\neq 0}$
"Cosinusoidal"	6.242 ± 0.002	0.434 ± 0.001	4.121 ± 0.024	0.005	0.014
"Bump"	5.852 ± 0.009	0.355 ± 0.001	4.607 ± 0.037	0.023	0.025
"Composite"	5.515 ± 0.010	0.331 ± 0.001	4.755 ± 0.026	0.027	0.019

Note. Coefficient values shown as fit ± uncertainty, where the uncertainty is obtained through linearized uncertainty propagation.

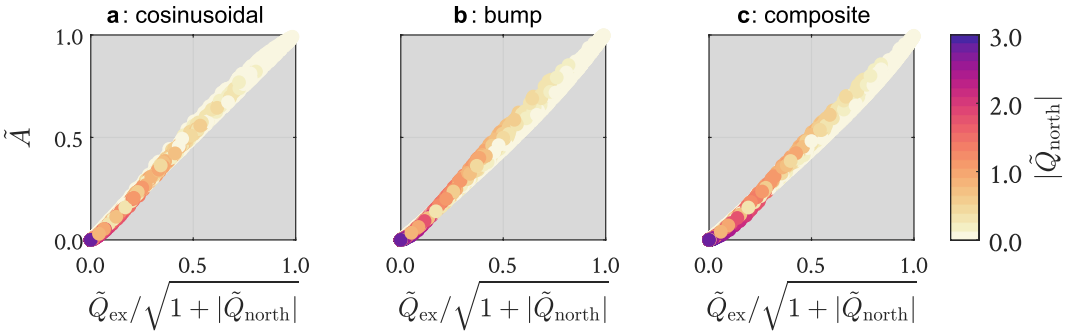

Figure 6. Relationship between the normalized exchange-zone area and the dimensionless discharge for the three domain shapes.

The relationship of Equation 47 suggests that in cases without a northern influx, the area of the hyporheic exchange zone closely scales with the normalized exchange flux and A_{north}. This implies that pronounced widening (i.e., large width differences $w_{max} - w_{min}$) leads to a larger exchange zone, but a greater ambient hydraulic gradient (I_x) would not have any effect on A_{ex}.

As intuitively expected, an influx on the northern hillslope boundary leads to a reduction of the exchange area. As outlined above, the influx from the northern hillslope leads to a reduction of the exchange flux, but the reduction of the area of the exchange zone is even bigger. One interpretation of that could be that an increase of $|\tilde{Q}_{north}|$ does not only shrink the exchange zone in the y-direction, but also reduces its extent along the southern boundary. For cases with $\tilde{Q}_{north} = 0$, on the other hand, the southern boundary of the exchange zone always covers the entire river and the occupied area varies only in the y-direction.

Similar to our analysis of Q_{ex}, we also provide a full global sensitivity analysis of A_{ex} using Sobol indices (Sobol', 1993, 2001) in Text S3.

3.3. Hyporheic Travel Times

For all simulated model scenarios, we calculated the distribution of normalized travel times as outlined above. Figure 7a, 7c and 7e show the resulting cumulative distribution functions for the three different domain shapes in the cases without northern influx. The plots for the cases with northern influx (see Text S6) show similar results and are subject to the same interpretations as done in the following.

We plotted the 5^{th}, 50^{th} and 95^{th} percentiles to highlight the spread across the collection of curves. It becomes clear that this spread is comparably small, and the travel-time distributions are similar, both for all distributions of a specific shape and between the three shapes. All curves show a sigmoidal behavior starting at a travel time of zero, approximately passing 50% cumulative probability at the mean travel time (determined from the area of and discharge through the exchange zone), and finally reaching 100% probability at about twice the mean travel time.

Table 4
Quality of the Empirical-Fit Metrics for the Area of the Exchange Zone

Shape	$RMSE_{area}$
"Cosinusoidal"	0.017
"Bump"	0.024
"Composite"	0.028

Note. The results are obtained for the sample of 3,000 model realizations per domain shape.

That the cumulative distribution function of travel times start at the origin is intuitively clear: an infinitesimally small travel time exists at the transition point along the river between losing and gaining conditions. The fact that all distributions nearly pass 50% at the mean travel time indicates that the median and mean travel times are almost identical. It is obvious that there must be a finite maximum travel time, which corresponds to the time that the water needs to travel along the bounding stream-line of the hyporheic exchange zone, which separates it from the remaining aquifer. This maximum travel time is about twice as large as t_{mean}. Altogether, this results in a symmetric travel-time distribution, which qualitatively differs from skewed travel-time distributions occurring in systems with stagnation points.

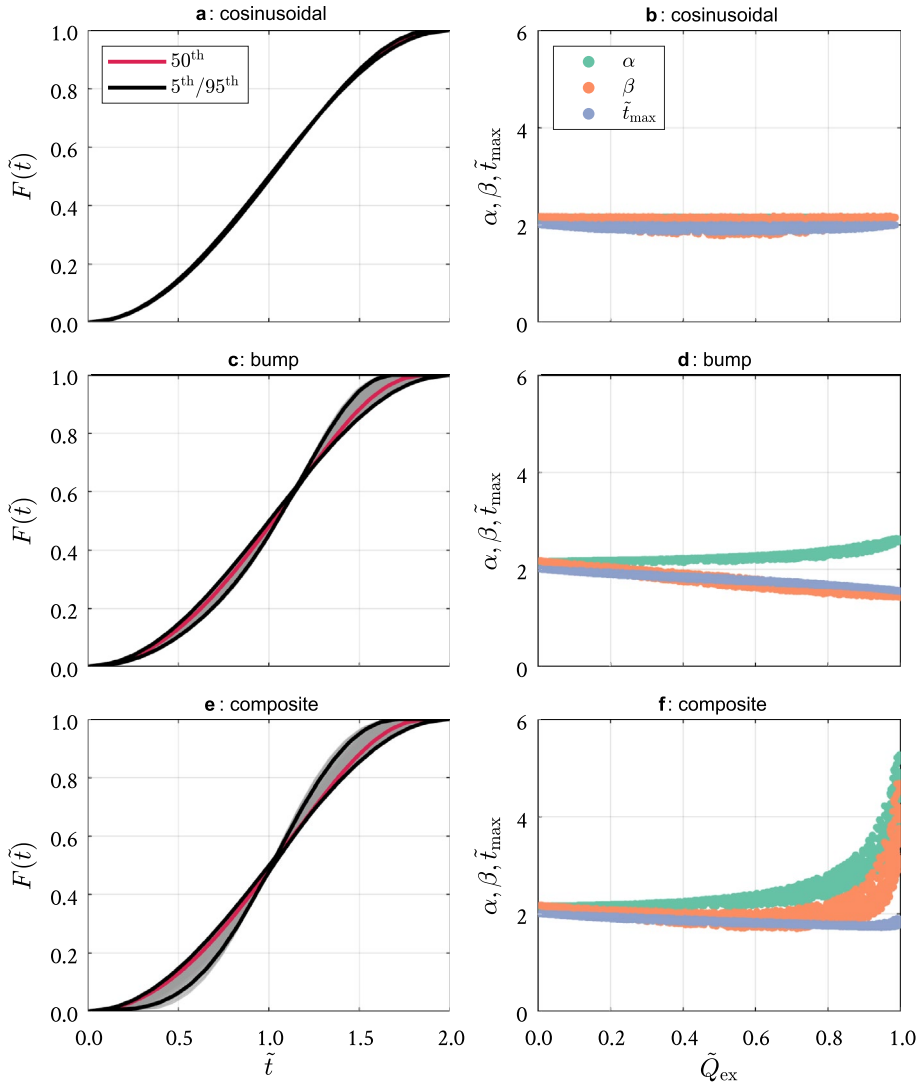

Figure 7. Travel-time distributions (a, c, and e) and coefficients of fitted beta distributions (b, d, and f) for the three shapes.

All curves shown in Figure 7 closely resemble Beta-distributions that are scaled in $\tilde{t}$-direction. Hence, we chose to fit the cumulative distribution functions with the Beta-distribution, in which the dimensionless time $\tilde{t}$ is scaled by the maximum time $\tilde{t}_{\max}$:

$$F(\tilde{t}) = \frac{B\left(\frac{\tilde{t}}{\tilde{t}_{\max}}; \alpha, \beta\right)}{B(1, \alpha, \beta)}, \tag{48}$$

where $B(\tilde{t}/\tilde{t}_{\max}, \alpha, \beta)$ is the incomplete beta function, whereas α and β are two shape parameters.

As a result of the fit, we obtain one set of values of α, β, and $\tilde{t}_{\max}$ for each simulation. Figures 7b, 7 and 7f show how these three fitted parameters depend on the dimensionless exchange flux $\tilde{Q}_{\text{ex}}$. Comparing the results of the three different shapes, it is remarkable that all shapes have the same parameter values for small dimensionless exchange fluxes, namely $\alpha \approx \beta \approx \tilde{t}_{\max} \approx 2$, implying a symmetric distribution with $t_{\max} \approx 2t_{\text{mean}}$ and a standard deviation of $t_{\text{mean}}/\sqrt{5}$. This is probably related to the fact that small values of $\tilde{Q}_{\text{ex}}$ indicate a large separation between the river and the northern boundary, where the specific shape of the boundary loses importance due to the diffusive nature of the groundwater flow equation. With increasing

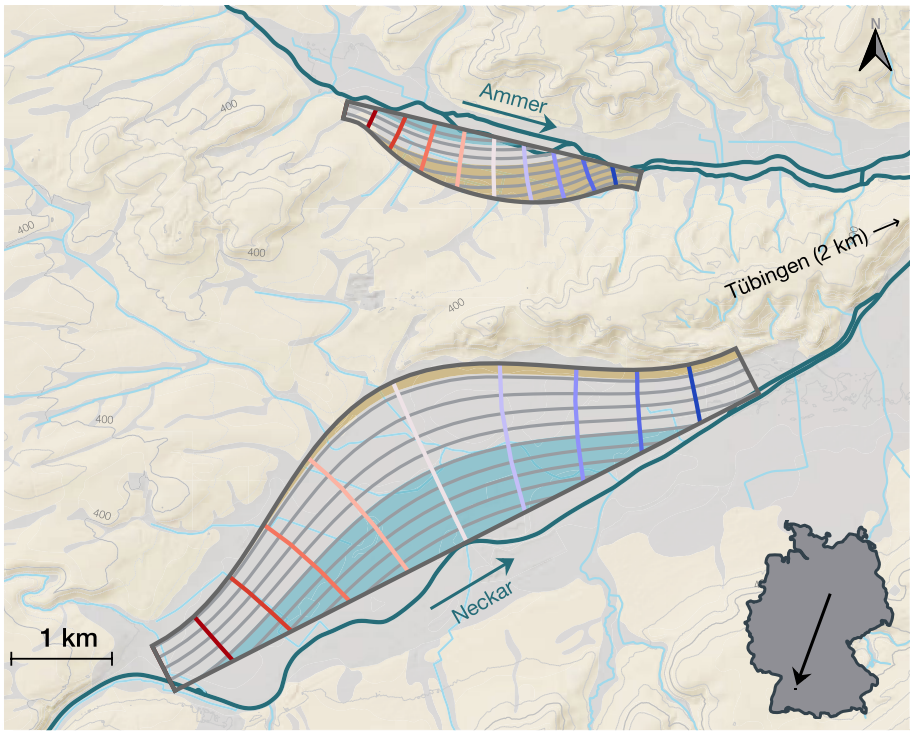

Figure 8. Map of the Ammer (case I, northern part) and Neckar (case II, southern part) floodplains near Tübingen, superimposed with example models. The model results are displayed as flow nets and translucent areas, similar to the styling of Figure 3. In accordance with that, bedrock deposits are shown in tan and floodplain materials are highlighted in light gray.

values of $\tilde{Q}_{ex}$ the fitted parameters begin to differ among the three different shapes. For the "cosinusoidal" case, the parameters barely change across the full range of the hyporheic exchange flux, whereas the other two shapes exhibit distinct trends. With increasing exchange flux, the maximum travel time drops from twice the mean travel time to a value of about $\tilde{t} = 1.6$ for both the "bump" and "composite" shape. This trend is accompanied by a change of the shape parameters α and β. For the "bump" shape, α and β start to deviate from each other with increasing exchange flux, creating an asymmetric travel-time distribution. In the "composite" models, asymmetry is also introduced (albeit to a smaller extent, as α and β change in the same direction), but the variance of the travel-time distribution decreases as α and β increase. Most likely, this is caused by the segment of constant width that the "composite" shape exhibits in the mid-section of the floodplain aquifer, as it encourages parallel flow paths in this part of the domain.

Overall however, the dominant behavior does neither depend on the domain shape nor on the magnitude of $\tilde{Q}_{ex}$.

3.4. Simplified Estimation of Hyporheic-Zone Properties for Two Adjacent Valleys

As a result of the previous proxy-model derivations, we propose a simplified estimation of hyporheic-zone properties, for a given setup. For illustrative purposes, we include two examples resembling the floodplains of the rivers Ammer (I) and Neckar (II) close to Tübingen, in south-western Germany. These two neighboring floodplain aquifers are exposed to similar geomorphological settings (e.g., their aspect ratios, the ambient hydraulic gradients and the degree of river channelization are comparable). However, they differ in their hydraulic properties and absolute size with the larger Neckar aquifer being dominated by sandy gravel resulting in larger transmissivities. The floodplain aquifer located in the adjacent Ammer valley is comparably small and consists of fine-grained material, which results in smaller transmissivities. Figure 8 shows a map of the two locations, as well as superimposed model results in the styling of Figure 3.

Table 5
Geometric and Hydraulic Parameters Used for the Two Example Calculations

Parameter	Symbol	Example I	Example II	Unit
Shape	–	Bump	Cosinusoidal	–
Domain length	L	$3.00 \cdot 10^3$	$6.50 \cdot 10^3$	m
Maximum width	w_{max}	$6.00 \cdot 10^2$	$1.75 \cdot 10^3$	m
Minimum width	w_{min}	$1.75 \cdot 10^2$	$5.00 \cdot 10^2$	m
Fixed heat at inlet	h_1	$3.49 \cdot 10^2$	$3.45 \cdot 10^2$	m
Fixed head at outlet	h_2	$3.41 \cdot 10^2$	$3.24 \cdot 10^2$	m
Transmissivity	$T_x = T_y$	$5.00 \cdot 10^{-5}$	$1.25 \cdot 10^{-2}$	m^2/s
Northern influx	q_{North}	$-2.50 \cdot 10^{-8}$	$-7.50 \cdot 10^{-7}$	m^2/s
Depth-integrated porosity	Φ	$2.00 \cdot 10^{-1}$	$7.50 \cdot 10^{-1}$	m
Average width	w_{mean}	$4.31 \cdot 10^2$	$1.12 \cdot 10^3$	m
Northern area	A_{north}	$7.69 \cdot 10^5$	$4.06 \cdot 10^6$	m^2

Just as stated in the introduction, we are interested in the hyporheic exchange flux, the extent of the associated exchange zone and the travel times of water parcels passing it. For the evaluation, we use the simplified proxy-equations:

1. Determine all geometric and hydraulic parameters. For the examples, we assume the values shown in Table 5.
2. Choose one of the three shape types that resembles the real shape best: we assume "bump" for the first example and "cosinusoidal" for the second one.
3. Read the coefficient values from Table 3: $a_1^{\mathrm{I}} = 5.852$, $a_2^{\mathrm{I}} = 0.355$ and $a_3^{\mathrm{I}} = 4.607$, and $a_1^{\mathrm{II}} = 6.242$, $a_2^{\mathrm{II}} = 0.434$ and $a_3^{\mathrm{II}} = 4.121$.
4. Evaluate Q_0 with Equation 40: $Q_0^{\mathrm{I}} = 5.68 \cdot 10^{-5}\,\mathrm{m}^3/\mathrm{s}$ and $Q_0^{\mathrm{II}} = 5.05 \cdot 10^{-2}\,\mathrm{m}^3/\mathrm{s}$.
5. Determine $\tilde{x}$ with Equation 42: $\tilde{x}^{\mathrm{I}} = 0.144$ and $\tilde{x}^{\mathrm{II}} = 0.173$.
6. Evaluate $\tilde{Q}_{north}$ with Equation 44: $\tilde{Q}_{north}^{\mathrm{I}} = -1.32$ and $\tilde{Q}_{north}^{\mathrm{II}} = -0.10$.
7. Determine $\tilde{Q}_{ex}$ either from Equation 45 or graphically from Figure 5: $\tilde{Q}_{ex}^{\mathrm{I}} = 0.308$ and $\tilde{Q}_{ex}^{\mathrm{II}} = 0.577$.
8. Find Q_{ex} by multiplying $\tilde{Q}_{ex}$ with Q_0: $Q_{ex}^{\mathrm{I}} = 1.74 \cdot 10^{-5}\,\mathrm{m}^3/\mathrm{s}$ and $Q_{ex}^{\mathrm{II}} = 2.91 \cdot 10^{-2}\,\mathrm{m}^3/\mathrm{s}$.
9. Determine the dimensionless area of the exchange zone either from Equation 47 or graphically from Figure 6: $\tilde{A}^{\mathrm{I}} = 0.202$ and $\tilde{A}^{\mathrm{II}} = 0.551$.
10. Find A_{ex} by multiplying $\tilde{A}$ with A_{north}: $A_{ex}^{\mathrm{I}} = 1.55 \cdot 10^5\,\mathrm{m}^2$ and $A_{ex}^{\mathrm{II}} = 2.24 \cdot 10^6\,\mathrm{m}^2$.
11. Obtain the mean travel time by diving the product of Φ and A_{ex} by Q_{ex}: $t_{mean}^{\mathrm{I}} = 1.78 \cdot 10^9\,\mathrm{s} \approx 56.5\mathrm{a}$ and $t_{mean}^{\mathrm{II}} = 5.76 \cdot 10^7\,\mathrm{s} \approx 1.8\mathrm{a}$.

The results of the simplified estimation compare reasonably well with the results of the semi-analytical solution (first case: $Q_{ex} = 1.74 \cdot 10^{-5}\,\mathrm{m}^3/\mathrm{s}$, $A_{ex} = 1.51 \cdot 10^5\,\mathrm{m}^2$ and 54.0a; second case: $Q_{ex} = 2.89 \cdot 10^{-2}\,\mathrm{m}^3/\mathrm{s}$, $A_{ex} = 2.62 \cdot 10^6\,\mathrm{m}^2$ and 2.2a). We see, that in both cases the absolute volumetric-exchange flux is small (e.g., compared to the discharge of the associated rivers, which is $0.5\mathrm{m}^3/\mathrm{s}$ and $7\mathrm{m}^3/\mathrm{s}$ under base-flow conditions). Comparing the results to the reported collection of surface-water/groundwater interaction fluxes reviewed by Cranswick and Cook (2015), the flux is basically negligible in the first case, while in the second case it operates at the lower end of the exchange-flux spectrum reported for rivers of similar discharge. In the first case (Ammer), the exchange-zone area is also relatively small. For the second case (Neckar), however, a large portion of the aquifer is taken up by the exchange zone. Both cases exhibit average travel times on

the order of years, which might be enough time for the infiltrated river water to lose its chemical signature and become very similar or indistinguishable from "true" groundwater (at least on the longer flow-paths).

Our proxy-equations require a value for the northern influx rate q_{north}, which might not be readily available for a specific site. For such cases, the following substitution might be helpful: q_{north} can be approximated by the length L_{hs} [L] of the connected hillslope and an estimated average groundwater recharge rate q_R [L/T] stemming from a water balance of a vertical two-dimensional hillslope slice:

$$q_{\text{north}} \approx L_{\text{hs}} \cdot q_R. \tag{49}$$

A schematic sketch illustrating this estimation is given in Text S7.

4. Conclusions

The widening and narrowing of river valleys due to varying bedrock geology, produces large-scale variations in the geometry of floodplain aquifers, which subsequently induce valley-scale lateral hyporheic exchange even for straight river reaches (see Figure 1). Estimating the size of the hyporheic exchange zone, the exchange flux, and the hyporheic travel-time distribution is relevant for groundwater management, river-water quality, and ecology. We have computed these properties by a semi-analytical modeling approach for idealized shapes of the floodplain aquifer. We found simple proxy-equations to decently approximate the geometry-driven steady-state exchange flux between floodplain aquifers and connected rivers, as well as the area covered by this hyporheic-exchange zone. The equations involve three empirical coefficients, which we have fitted for three different shapes of the floodplain aquifer. Our semi-analytical solution for the described problem provides the hydraulic-head, specific-discharge, and stream-function values throughout the domain. This information can be used to determine fluxes between different points, to construct dividing streamlines, to highlight zones of different hydrological origin and destination, and to determine travel times.

Our main conclusions from investigating the behavior of valley-scale lateral hyporheic exchange across the geometric and hydraulic parameter space are:

1. The maximum width-difference, the ambient hydraulic gradient, and the longitudinal transmissivity of the floodplain aquifer exert a linear control on the potential maximum exchange flux Q_0 between the river and the floodplain.
2. The ratio of the actual exchange flux Q_{ex} to Q_0 depends non-linearly on the aspect ratio of the domain (w_{mean}/L), which is the ratio of the floodplain width to the channel length. Large aspect ratios lead to less hyporheic exchange.
3. Horizontal hydraulic anisotropy ($T_x \neq T_y$) can act as a scaling factor for the aspect ratio of the domain, controlling the ease of which water can be drawn from the river.
4. Groundwater influx from the hillslope q_{north} exerts a strong control on the size of the exchange zone, where increasing q_{north} effectively pushes it toward the river while also reducing its longitudinal extent.
5. Travel-time distributions of hyporheic exchange water approximately follow Beta-distributions.

The applicability of the presented model to real case studies is of course limited: Real systems are affected by transient forcings and are subject to three-dimensional heterogeneity. Furthermore, our model only considers two-dimensional divergence-free groundwater flow and thereby assumes that the aquifer and the river are connected across the full aquifer depth, which is often not the case in real systems. Nonetheless, our expressions are useful for quick estimations of the lateral exchange flux in cases with little known information. For example, our results can be used to decide which of several sites is most promising for targeted measurements of hyporheic exchange if budget restrictions limit field investigations to one site. Actual field data might then be used to calibrate and validate flow models (the presented one, or a more complex model) in order to simulate and quantify the hyporheic exchange more accurately.

Other relevant questions, for example, whether the groundwater sampling point at a given location lies within the hyporheic-exchange zone can be answered by the semi-analytical method, but we have not developed proxy models for them. Future work may expand on that. Furthermore, it might be interesting to extend the semi-analytical solution to account for river meanders or non-uniform slopes. It might also be

worthwhile to analyze the effects of asymmetric northern boundaries/influxes (i.e., $f_B(x)$ and $q_{\text{north}}(x)$) on the hyporheic exchange zone.

Data Availability Statement

The model source code used to generate all data of this study is available in form of a repository at https://osf.io/fykr9/ (Allgeier et al., 2021). It comes in a command-line interface Matlab version and an interactive Python Bokeh application (Bokeh Development Team, 2021). The authors provide this interactive tool also as a free online service (https://jonasallgeier.github.io/fpsimple) that can be accessed and executed in all common web browsers.

Acknowledgments
This research was funded by the German Research Foundation (DFG) in the framework of the Research Training Group GRK 1829 "Integrated Hydrosystem Modelling" and the Collaborative Research Center SFB 1253 CAMPOS—Catchments as Reactors (Grant Agreements GRK 1829/2 and SFB 1253/1 2017). The authors acknowledge support by the Open Access Publishing Fund of the University of Tübingen. Finally, the authors thank three anonymous reviewers for their valuable feedback which improved the manuscript. Open access funding enabled and organized by Projekt DEAL.

References

Allgeier, J., Martin, S., & Cirpka, O. A. (2021). *Code for the systematic evaluation of geometry-driven lateral river-groundwater exchange in floodplains*. https://doi.org/10.17605/OSFIO/FYKR9

Bakker, M. (1999). Simulating groundwater flow in multi-aquifer systems with analytical and numerical Dupuit-models. *Journal of Hydrology*, *222*(1), 55–64. https://doi.org/10.1016/S0022-1694(99)00089-X

Bakker, M. (2006). An analytic element approach for modeling polygonal inhomogeneities in multi-aquifer systems. *Advances in Water Resources*, *29*(10), 1546–1555. https://doi.org/10.1016/j.advwatres.2005.11.005

Bakker, M., & Strack, O. D. L. (2003). Analytic elements for multiaquifer flow. *Journal of Hydrology*, *271*(1), 119–129. https://doi.org/10.1016/S0022-1694(02)00319-0

Barnes, R., & Janković, I. (1999). Two-dimensional flow through large numbers of circular inhomogeneities. *Journal of Hydrology*, *226*(3), 204–210. https://doi.org/10.1016/S0022-1694(99)00142-0

Barthel, R., & Banzhaf, S. (2016). Groundwater and surface water interaction at the regional-scale – A review with focus on regional integrated models. *Water Resources Management*, *30*(1), 1–32. https://doi.org/10.1007/s11269-015-1163-z

Bates, P. D., Stewart, M. D., Desitter, A., Anderson, M. G., Renaud, J.-P., & Smith, J. A. (2000). Numerical simulation of floodplain hydrology. *Water Resources Research*, *36*(9), 2517–2529. https://doi.org/10.1029/2000WR900102

Baxter, C. V., Frissell, C. A., & Hauer, F. R. (1999). Geomorphology, logging roads, and the distribution of bull trout spawning in a forested river basin: Implications for management and conservation. *Transactions of the American Fisheries Society*, *14*. https://doi.org/10.1577/1548-8659(1999)128<0854:glratd>2.0.co;2

Bear, J (1972). *Dynamics of fluids in porous media*. New York: American Elsevier Pub. Co. https://agris.fao.org/agris-search/search.do?recordID=US201300010992

Boano, F., Camporeale, C., Revelli, R., & Ridolfi, L. (2006). Sinuosity-driven hyporheic exchange in meandering rivers. *Geophysical Research Letters*, *33*(18), L18406. https://doi.org/10.1029/2006GL027630

Boano, F., Harvey, J. W., Marion, A., Packman, A. I., Revelli, R., Ridolfi, L., & Wörman, A. (2014). Hyporheic flow and transport processes: Mechanisms, models, and biogeochemical implications. *Reviews of Geophysics*, *52*(4), 603–679. https://doi.org/10.1002/2012RG000417

Boano, F., Revelli, R., & Ridolfi, L. (2009). Quantifying the impact of groundwater discharge on the surface–subsurface exchange. *Hydrological Processes*, *23*(15), 2108–2116. https://doi.org/10.1002/hyp.7278

Bokeh Development Team. (2021). *Bokeh: Python library for interactive visualization*[Manual]. https://bokeh.org/

Boyraz, U., & Kazezyılmaz-Alhan, C. M. (2013). An investigation on the effect of geometric shape of streams on stream/ground water interactions and ground water flow. *Hydrology Research*, *45*(4–5), 575–588. https://doi.org/10.2166/nh.2013.057

Boyraz, U., & Kazezyılmaz-Alhan, C. M. (2017). Solutions for groundwater flow with sloping stream boundary: Analytical, numerical and experimental models. *Hydrology Research*, *49*(4), 1120–1130. https://doi.org/10.2166/nh.2017.264

Boyraz, U., & Kazezyılmaz-Alhan, C. M. (2021). An analytical solution for groundwater flow incorporating the effect of water bodies with sloping surfaces. *Hydrological Sciences Journal*, *66*. https://doi.org/10.1080/02626667.2021.1925675

Brookes, A. (1987). The distribution and management of channelized streams in Denmark. *Regulated Rivers: Research & Management*, *1*(1), 3–16. https://doi.org/10.1002/rrr.3450010103

Buffington, J. M., & Tonina, D. (2009). Hyporheic exchange in mountain rivers II: Effects of channel morphology on mechanics, scales, and rates of exchange. *Geography Compass*, *3*(3), 1038–1062. https://doi.org/10.1111/j.1749-8198.2009.00225.x

Cardenas, M. B. (2009a). A model for lateral hyporheic flow based on valley slope and channel sinuosity. *Water Resources Research*, *45*(1), W01501. https://doi.org/10.1029/2008WR007442

Cardenas, M. B. (2009b). Stream-aquifer interactions and hyporheic exchange in gaining and losing sinuous streams. *Water Resources Research*, *45*(6), W06429. https://doi.org/10.1029/2008WR007651

Castro, N. M., & Hornberger, G. M. (1991). Surface-subsurface water interactions in an alluviated mountain stream channel. *Water Resources Research*, *27*(7), 1613–1621. https://doi.org/10.1029/91wr00764

Cheng, J., & Druzdzel, M. J. (2013). *Computational investigation of low-discrepancy sequences in simulation algorithms for Bayesian networks*. http://arxiv.org/abs/1301.3841

Clément, J.-C., Aquilina, L., Bour, O., Plaine, K., Burt, T. P., & Pinay, G. (2003). Hydrological flowpaths and nitrate removal rates within a riparian floodplain along a fourth-order stream in Brittany (France). *Hydrological Processes*, *17*(6), 1177–1195. https://doi.org/10.1002/hyp.1192

Clilverd, H., Thompson, J., Heppell, C., Sayer, C., & Axmacher, J. (2013). River–floodplain hydrology of an embanked lowland Chalk river and initial response to embankment removal. *Hydrological Sciences Journal*, *58*(3), 627–650. https://doi.org/10.1080/02626667.2013.774089

Cloke, H. L., Renaud, J. P., Claxton, A. J., McDonnell, J. J., Anderson, M. G., Blake, J. R., & Bates, P. D. (2003). The effect of model configuration on modelled hillslope–riparian interactions. *Journal of Hydrology*, *279*(1), 167–181. https://doi.org/10.1016/S0022-1694(03)00177-X

Cook, P. G. (2015). Quantifying river gain and loss at regional scales. *Journal of Hydrology*, *531*, 749–758. https://doi.org/10.1016/j.jhydrol.2015.10.052

Craig, J. R. (2008). Analytical solutions for 2D topography-driven flow in stratified and syncline aquifers. *Advances in Water Resources*, *31*(8), 1066–1073. https://doi.org/10.1016/j.advwatres.2008.04.011
Cranswick, R. H., & Cook, P. G. (2015). Scales and magnitude of hyporheic, river–aquifer and bank storage exchange fluxes. *Hydrological Processes*, *29*(14), 3084–3097. https://doi.org/10.1002/hyp.10421
Dall'O', M., Kluge, W., & Bartels, F. (2001). FEUWAnet: A multi-box water level and lateral exchange model for riparian wetlands. *Journal of Hydrology*, *250*(1), 40–62. https://doi.org/10.1016/S0022-1694(01)00401-2
Darcy, H. P. G. (1856). *Les fontaines publiques de la ville de Dijon. Exposition et application des principes à suivre et des formules à employer dans les questions de distribution d'eau etc*. V. Dalamont.
Fabian, M. W., Endreny, T. A., Bottacin-Busolin, A., & Lautz, L. K. (2011). Seasonal variation in cascade-driven hyporheic exchange, northern Honduras. *Hydrological Processes*, *25*(10), 1630–1646. https://doi.org/10.1002/hyp.7924
Fitts, C. R. (2010). Modeling aquifer systems with analytic elements and subdomains. *Water Resources Research*, *46*(7), W07521. https://doi.org/10.1029/2009WR008331
Fotherby, L. M. (2009). Valley confinement as a factor of braided river pattern for the Platte River. *Geomorphology*, *103*(4), 562–576. https://doi.org/10.1016/j.geomorph.2008.08.001
Fritz, K. M., Schofield, K. A., Alexander, L. C., McManus, M. G., Golden, H. E., Lane, C. R., et al. (2018). Physical and chemical connectivity of streams and Riparian wetlands to downstream waters: A Synthesis. *JAWRA Journal of the American Water Resources Association*, *54*(2), 323–345. https://doi.org/10.1111/1752-1688.12632
Gibbs, J. W. (1898). Fourier's series. *Nature*, *59*(1522), 200. https://doi.org/10.1038/059200b0
Gomez, J. D., Wilson, J. L., & Cardenas, M. B. (2012). Residence time distributions in sinuosity-driven hyporheic zones and their biogeochemical effects. *Water Resources Research*, *48*(9), W09533. https://doi.org/10.1029/2012WR012180
Gomez-Velez, J. D., Wilson, J. L., Cardenas, M. B., & Harvey, J. W. (2017). Flow and residence times of dynamic river bank storage and sinuosity-driven hyporheic exchange. *Water Resources Research*, *53*(10), 8572–8595. https://doi.org/10.1002/2017WR021362
Gooseff, M. N., McKnight, D. M., Runkel, R. L., & Vaughn, B. H. (2003). Determining long time-scale hyporheic zone flow paths in Antarctic streams. *Hydrological Processes*, *17*(9), 1691–1710. https://doi.org/10.1002/hyp.1210
Halton, J. H. (1960). On the efficiency of certain quasi-random sequences of points in evaluating multi-dimensional integrals. *Numerische Mathematik*, *2*(1), 84–90. https://doi.org/10.1007/BF01386213
Harvey, J. W., & Bencala, K. E. (1993). The effect of streambed topography on surface-subsurface water exchange in mountain catchments. *Water Resources Research*, *29*(1), 89–98. https://doi.org/10.1029/92wr01960
Hayashi, M., & Rosenberry, D. O. (2002). Effects of ground water exchange on the hydrology and ecology of surface water. *Groundwater*, *40*(3), 309–316. https://doi.org/10.1111/j.1745-6584.2002.tb02659.x
Helton, A. M., Poole, G. C., Payn, R. A., Izurieta, C., & Stanford, J. A. (2012). Scaling flow path processes to fluvial landscapes: An integrated field and model assessment of temperature and dissolved oxygen dynamics in a river-floodplain-aquifer system. *Journal of Geophysical Research*, *117*(G4), G00N14. https://doi.org/10.1029/2012JG002025
Hewitt, E., & Hewitt, R. E. (1979). The Gibbs-Wilbraham phenomenon: An episode in Fourier analysis. *Archive for History of Exact Sciences*, *21*(2), 129–160. https://doi.org/10.1007/BF00330404
Hill, A. R. (1990). Ground water flow paths in relation to nitrogen chemistry in the near-stream zone. *Hydrobiologia*, *206*(1), 39–52. https://doi.org/10.1007/BF00018968
Hill, A. R. (2019). Groundwater nitrate removal in riparian buffer zones: A review of research progress in the past 20 years. *Biogeochemistry*, *143*(3), 347–369. https://doi.org/10.1007/s10533-019-00566-5
Huang, P., & Chui, T. F. M. (2018). Empirical equations to predict the characteristics of hyporheic exchange in a pool-riffle sequence. *Groundwater*, *56*(6), 947–958. https://doi.org/10.1111/gwat.12641
Janković, I., & Barnes, R. (1999). Three-dimensional flow through large numbers of spheroidal inhomogeneities. *Journal of Hydrology*, *226*(3), 224–233. https://doi.org/10.1016/S0022-1694(99)00141-9
Kalbus, E., Reinstorf, F., & Schirmer, M. (2006). Measuring methods for groundwater – Surface water interactions: A review. *Hydrology and Earth System Sciences*, *10*(6), 873–887. https://doi.org/10.5194/hess-10-873-2006
Kasahara, T., & Wondzell, S. M. (2003). Geomorphic controls on hyporheic exchange flow in mountain streams. *Water Resources Research*, *39*(1), 3–1. https://doi.org/10.1029/2002WR001386
Kocis, L., & Whiten, W. J. (1997). Computational investigations of low-discrepancy sequences. *ACM Transactions on Mathematical Software*, *23*(2), 266–294. https://doi.org/10.1145/264029.264064
Langhoff, J. H., Rasmussen, K. R., & Christensen, S. (2006). Quantification and regionalization of groundwater–surface water interaction along an alluvial stream. *Journal of Hydrology*, *320*(3), 342–358. https://doi.org/10.1016/j.jhydrol.2005.07.040
Lewandowski, J., Arnon, S., Banks, E., Batelaan, O., Betterle, A., Broecker, T., et al. (2019). Is the hyporheic zone relevant beyond the scientific community? *Water*, *11*(11), 2230. https://doi.org/10.3390/w11112230
Li, P., Stagnitti, F., & Das, U. (1996). A new analytical solution for Laplacian porous-media flow with arbitrary boundary shapes and conditions. *Mathematical and Computer Modelling*, *24*(10), 3–19. https://doi.org/10.1016/S0895-7177(96)00160-4
Magliozzi, C., Grabowski, R., Packman, A. I., & Krause, S. (2017). Scaling down hyporheic exchange flows: From catchments to reaches. *Hydrology and Earth System Sciences Discussions*, 1–53. https://doi.org/10.5194/hess-2016-683
Magliozzi, C., Grabowski, R. C., Packman, A. I., & Krause, S. (2018). Toward a conceptual framework of hyporheic exchange across spatial scales. *Hydrology and Earth System Sciences*, *22*(12), 6163–6185. https://doi.org/10.5194/hess-22-6163-2018
Mallard, J., McGlynn, B., & Covino, T. (2014). Lateral inflows, stream-groundwater exchange, and network geometry influence stream water composition. *Water Resources Research*, *50*(6), 4603–4623. https://doi.org/10.1002/2013WR014944
Martin, S., Klingler, S., Dietrich, P., Leven, C., & Cirpka, O. A. (2020). Structural controls on the hydrogeological functioning of a floodplain. *Hydrogeology Journal*, *28*(8), 2675–2696. https://doi.org/10.1007/s10040-020-02225-8
Nagel, D. E., Buffington, J. M., Parkes, S. L., Wenger, S., & Goode, J. R. (2014). *A landscape scale valley confinement algorithm: Delineating unconfined valley bottoms for geomorphic, aquatic, and riparian applications* (General Technical Report No. RMRS-GTR-321). Fort Collins, CO: U.S. Department of Agriculture, Forest Service, Rocky Mountain Research Station. https://doi.org/10.2737/RMRS-GTR-321
Ó Dochartaigh, B. É., Archer, N. A. L., Peskett, L., MacDonald, A. M., Black, A. R., Auton, C. A., et al. (2019). Geological structure as a control on floodplain groundwater dynamics. *Hydrogeology Journal*, *27*(2), 703–716. https://doi.org/10.1007/s10040-018-1885-0
Ohara, N., Holbrook, W. S., Yamatani, K., Flinchum, B. A., & Clair, J. T. S. (2018). Spatial delineation of riparian groundwater within alluvium deposit of mountainous region using Laplace equation. *Hydrological Processes*, *32*(1), 30–38. https://doi.org/10.1002/hyp.11395
Powers, W. L. (1966). *Solution of some theoretical soil drainage problems by generalized orthonormal functions* (p. 254). Iowa State University.

Powers, W. L., Kirkham, D., & Snowden, G. (1967). Orthonormal function tables and the seepage of steady rain through soil bedding. *Journal of Geophysical Research*, *72*(24), 6225–6237. https://doi.org/10.1029/JZ072i024p06225
Ray, S. (2020). A reconstruction-based Chebyshev-collocation method for the Poisson equation: An accurate treatment of the Gibbs-Wilbraham phenomenon on irregular interfaces. *Journal of Computational Physics*, *20*. https://doi.org/10.1016/j.jcp.2020.109559
Read, W. W. (2007). An analytic series method for Laplacian problems with mixed boundary conditions. *Journal of Computational and Applied Mathematics*, *209*(1), 22–32. https://doi.org/10.1016/j.cam.2006.10.088
Ren, J., Zhang, W., Yang, J., & Zhou, Y. (2019). Using water temperature series and hydraulic heads to quantify hyporheic exchange in the riparian zone. *Hydrogeology Journal*, *27*(4), 1419–1437. https://doi.org/10.1007/s10040-019-01934-z
Revelli, R., Boano, F., Camporeale, C., & Ridolfi, L. (2008). Intra-meander hyporheic flow in alluvial rivers. *Water Resources Research*, *44*(12), W12428. https://doi.org/10.1029/2008WR007081
Runge, C. (1901). Über empirische Funktionen und die Interpolation zwischen äquidistanten Ordinaten. *Zeitschrift für Mathematik und Physik*, *46*(224–243), 20.
Sobol', I. M. (1993). Sensitivity analysis for non-linear mathematical models. *Mathematical Modelling in Civil Engineering*, *1*, 407–414.
Sobol', I. M. (2001). Global sensitivity indices for nonlinear mathematical models and their Monte Carlo estimates. *Mathematics and Computers in Simulation*, *55*(1), 271–280. https://doi.org/10.1016/S0378-4754(00)00270-6
Strack, O. D. (1989). *Groundwater mechanics*. Prentice Hall.
Strack, O. D. L. (2003). Theory and applications of the analytic element method. *Reviews of Geophysics*, *41*(2), 1005. https://doi.org/10.1029/2002RG000111
Strack, O. D. L. (2017). *Analytical groundwater mechanics*. Cambridge University Press. https://doi.org/10.1017/9781316563144
Strack, O. D. L. (2018). Limitless analytic elements. *Water Resources Research*, *54*(2), 1174–1190. https://doi.org/10.1002/2017WR022117
Strack, O. D. L., & Nevison, P. R. (2015). Analytic elements of smooth shapes. *Journal of Hydrology*, *529*, 231–239. https://doi.org/10.1016/j.jhydrol.2015.07.001
Suribhatla, R., Bakker, M., Bandilla, K., & Janković, I. (2004). Steady two-dimensional groundwater flow through many elliptical inhomogeneities. *Water Resources Research*, *40*(4), W04202. https://doi.org/10.1029/2003WR002718
Tonina, D., & Buffington, J. M. (2009). Hyporheic Exchange in Mountain Rivers I: Mechanics and Environmental Effects: Mechanics of hyporheic exchange. *Geography Compass*, *3*(3), 1063–1086. https://doi.org/10.1111/j.1749-8198.2009.00226.x
Tóth, J. (1963). A theoretical analysis of groundwater flow in small drainage basins. *Journal of Geophysical Research*, *68*(16), 4795–4812. https://doi.org/10.1029/JZ068i016p04795
Triska, F. J., Duff, J. H., & Avanzino, R. J. (1993). The role of water exchange between a stream channel and its hyporheic zone in nitrogen cycling at the terrestrial-aquatic interface. *Hydrobiologia*, *18*. https://doi.org/10.1007/bf00007177
Vaux, W. G. (1968). Intragravel flow and interchange of water in a streambed. *Fishery Bulletin of the Fish and Wildlife Service*, *66*(3), 479–489.
Vidon, P. G., Welsh, M. K., & Hassanzadeh, Y. T. (2019). Twenty years of riparian zone research (1997–2017): Where to next? *Journal of Environmental Quality*, *48*(2), 248–260. https://doi.org/10.2134/jeq2018.01.0009
Wagner, F. H., & Bretschko, G. (2003). Riparian trees and flow paths between the hyporheic zone and groundwater in the Oberer Seebach, Austria. *International Review of Hydrobiology*, *88*(2), 129–138. https://doi.org/10.1002/iroh.200390009
Ward, A. S. (2016). The evolution and state of interdisciplinary hyporheic research. *WIREs Water*, *3*(1), 83–103. https://doi.org/10.1002/wat2.1120
Ward, A. S., Gooseff, M. N., & Singha, K. (2010). Imaging hyporheic zone solute transport using electrical resistivity. *Hydrological Processes*, *24*(7), 948–953. https://doi.org/10.1002/hyp.7672
Ward, A. S., & Packman, A. I. (2019). Advancing our predictive understanding of river corridor exchange. *Wiley Interdisciplinary Reviews: Water*, *6*(1), e1327. https://doi.org/10.1002/wat2.1327
Ward, A. S., Schmadel, N. M., Wondzell, S. M., Harman, C., Gooseff, M. N., & Singha, K. (2016). Hydrogeomorphic controls on hyporheic and riparian transport in two headwater mountain streams during base flow recession. *Water Resources Research*, *52*(2), 1479–1497. https://doi.org/10.1002/2015WR018225
Welch, C., Harrington, G. A., & Cook, P. G. (2015). Influence of Groundwater Hydraulic Gradient on Bank Storage Metrics. *Groundwater*, *53*(5), 782–793. https://doi.org/10.1111/gwat.12283
Wilbraham, H. (1848). On a certain periodic function. *The Cambridge and Dublin Mathematical Journal*, *3*, 198–201.
Winter, T. C., Harvey, J. W., Franke, O. L., & Alley, W. M. (1998). Ground Water and Surface Water: A Single Resource (Vol. 1139). US geological Survey.
Woessner, W. W. (2000). Stream and fluvial plain ground water interactions: Rescaling hydrogeologic thought. *Ground Water*, *38*(3), 423–429. https://doi.org/10.1111/j.1745-6584.2000.tb00228.x
Zachara, J. M., Chen, X., Song, X., Shuai, P., Murray, C., & Resch, C. T. (2020). Kilometer-scale hydrologic exchange flows in a gravel bed river corridor and their implications to solute migration. *Water Resources Research*, *56*(2), e2019WR025258. https://doi.org/10.1029/2019WR025258
Zhang, Y., Wang, J., Yang, P., & Xie, S. (2017). Movement of lateral hyporheic flow between stream and groundwater. *Science China Earth Sciences*, *60*(11), 2033–2040. https://doi.org/10.1007/s11430-016-9103-9
Zlotnik, V. A., Cardenas, M. B., & Toundykov, D. (2011). Effects of multiscale anisotropy on basin and hyporheic groundwater flow. *Groundwater*, *49*(4), 576–583. https://doi.org/10.1111/j.1745-6584.2010.00775.x